The Astrophysical Journal, 1003:19 (20pp), 2026 May 20 https://doi.org/10.3847/1538-4357/ae6245

SN 2019vxm: A Shocking Coincidence between Fermi and TESS

Zachary G. Lane[1], Ryan Ridden-Harper[1], Sofia Rest[2], Armin Rest[3,4], Conor L. Ransome[5,6], Qinan Wang[7], Clarinda Montilla[1], Micaela Steed[1,8], Igor Andreoni[9], Patrick Armstrong[10,11,12], Peter J. Brown[13], Jeffrey Cooke[14,15], David A. Coulter[3,4], Ori Fox[4], James Freeburn[16,17], Marco Galoppo[1], Avishay Gal-Yam[18], Jared A. Goldberg[19,20], Christopher Harvey-Hawes[1], Daichi Hiramatsu[21], Rebekah Hounsell[22,23], D. Andrew Howell[24,25], Brayden Leicester[1], Klára Lelkes[26,27], Itai Linial[28], Jaime Luisi[1], Curtis McCully[24,25], László Molnár[26,27], Thomas Moore[4], Pierre Mourier[1], Anya E. Nugent[6], David O'Neill[29,30], Hugh Roxburgh[1,31], Koji Shukawa[3], Stephen J. Smartt[32,33], Nathan Smith[5], Ken W. Smith[32,33], Bhagya M. Subrayan[5], Sebastian Vergara Carrasco[1], V. Ashley Villar[6,34], József Vinkó[26,27,35], Tal Wasserman[18], Yossef Zenati[3,36,37], and Erez A. Zimmerman[18]

[1] School of Physical and Chemical Sciences—Te Kura Matū, University of Canterbury, Private Bag 4800, Christchurch 8140, Aotearoa, New Zealand; zachary.lane@pg.canterbury.ac.nz
[2] Department of Computer Science, The Johns Hopkins University, Baltimore, MD 21218, USA
[3] William H. Miller III Department of Physics & Astronomy, Johns Hopkins University, 3400 North Charles Street, Baltimore, MD 21218, USA
[4] Space Telescope Science Institute, 3700 San Martin Drive, Baltimore, MD 21218, USA
[5] Steward Observatory, University of Arizona, 933 North Cherry Avenue, Tucson, AZ 85721, USA
[6] Center for Astrophysics | Harvard & Smithsonian, Cambridge, MA 02138, USA
[7] Department of Physics and Kavli Institute for Astrophysics and Space Research, Massachusetts Institute of Technology, Cambridge, MA 02139, USA
[8] Department of Physics, University of Auckland, Private Bag 92019, Auckland, Aotearoa, New Zealand
[9] Department of Physics and Astronomy, University of North Carolina at Chapel Hill, Chapel Hill, NC 27599-3255, USA
[10] The Research School of Astronomy and Astrophysics, Australian National University, ACT 2601, Australia
[11] E.O. Lawrence Berkeley National Laboratory, 1 Cyclotron Road, Berkeley, CA 94720, USA
[12] The Research School of Astronomy and Astrophysics, The Australian National University, Canberra, ACT 2611, Australia
[13] George P. and Cynthia Woods Mitchell Institute for Fundamental Physics and Astronomy, Department of Physics and Astronomy, Texas A&M University, College Station, TX 77843, USA
[14] Centre for Astrophysics and Supercomputing, Swinburne University of Technology, John Street, Hawthorn, VIC 3122, Australia
[15] ARC Centre of Excellence for Gravitational Wave Discovery (OzGrav), John Street, Hawthorn, VIC 3122, Australia
[16] Department of Physics and Astronomy, University of North Carolina, Chapel Hill, NC 27599, USA
[17] Sydney Institute for Astronomy, School of Physics, The University of Sydney, NSW 2006, Australia
[18] Department of Particle Physics and Astrophysics, Weizmann Institute of Science, 76100 Rehovot, Israel
[19] Department of Physics and Astronomy, Michigan State University, East Lansing, MI 48824, USA
[20] Center for Computational Astrophysics, Flatiron Institute, 162 5th Avenue, New York, NY 10010, USA
[21] Department of Astronomy, University of Florida, 211 Bryant Space Science Center, Gainesville, FL 32611-2055, USA
[22] University of Maryland Baltimore County, 1000 Hilltop Circle, Baltimore, MD 21250, USA
[23] NASA Goddard Space Flight Center, 8800 Greenbelt Road, Greenbelt, MD 20771, USA
[24] Las Cumbres Observatory, 6740 Cortona Drive, Suite 102, Goleta, CA 93117-5575, USA
[25] Department of Physics, University of California, Santa Barbara, CA 93106-9530, USA
[26] HUN-REN CSFK, Konkoly Observatory, MTA Centre of Excellence, Konkoly Thege Miklós út 15-17, Budapest, 1121, Hungary
[27] ELTE Eötvös Loránd University, Institute of Physics and Astronomy, Pázmány Péter sétány 1, Budapest, Hungary
[28] Columbia Astrophysics Laboratory, Columbia University, New York, NY 10027, USA
[29] School of Physics and Astronomy, University of Birmingham, Birmingham B15 2TT, UK
[30] Institute for Gravitational Wave Astronomy, University of Birmingham, Birmingham B15 2TT, UK
[31] International Centre for Radio Astronomy Research, Curtin University, Bentley, WA 6102, Australia
[32] Astrophysics Research Centre, School of Mathematics and Physics, Queen's University Belfast, Belfast BT7 1NN, UK
[33] Astrophysics sub-Department, Department of Physics, University of Oxford, Keble Road, Oxford, OX1 3RH, UK
[34] The NSF AI Institute for Artificial Intelligence and Fundamental Interactions, USA
[35] Department of Experimental Physics, University of Szeged, Dm´ tér 9, Szeged, 6720, Hungary
[36] Department of Natural Sciences, The Open University of Israel, Ra'anana 4353701, Israel
[37] Astrophysics Research Center of the Open University (ARCO), Ra'anana 4353701, Israel
Received 2025 November 19; revised 2026 March 22; accepted 2026 April 10; published 2026 May 11

Abstract

Shock breakout and, in some cases, jet-driven high-energy emission are increasingly recognized as key signatures of the earliest phases of core-collapse supernovae, especially in Type IIn systems due to their dense, interaction-dominated circumstellar environments. We present a comprehensive photometric analysis of SN 2019vxm, a long-duration, luminous Type IIn supernova, $M_V = -21.41 \pm 0.05$ mag, observed from X-ray to near-infrared. SN 2019vxm is the first superluminous supernovae Type IIn to be caught with well-sampled TESS photometric data on the rise and has a convincing coincident X-ray source at the time of first light. The high-cadence TESS light curve captures the early-time rise, which is well described by a broken power law with an index of $n = 1.41 \pm 0.04$, significantly shallower than the canonical $n = 2$ behavior. From this, we constrain the time of

first light to within 7.2 hr. We identify a spatial and temporal coincidence between SN 2019vxm and the hard X-ray/gamma-ray transient GRB 191117A, corresponding to a 3.3σ association confidence. Both the short-duration X-ray event and the lightcurve modeling are consistent with shock breakout into a dense, asymmetric circumstellar medium, indicative of a massive, compact progenitor such as a luminous blue variable transitioning to Wolf–Rayet phase embedded in a clumpy, asymmetric environment.

Unified Astronomy Thesaurus concepts: Supernovae (1668); Core-collapse supernovae (304); Transient sources (1851); X-ray bursts (1814); High energy astrophysics (739)

1. Introduction

Type IIn are a hydrogen-rich subclass of supernovae (SNe) that are characterized by their narrow spectral features (often with velocity dispersions $\sim$100 km s^{-1}) and the presence of hydrogen in the spectrum (I. Arcavi 2017). Unlike most other classifications of SNe, Type IIns are not associated with a specific explosion mechanism or progenitor system but instead significant interaction with the circumstellar medium (CSM) in the surrounding environment (E. M. Schlegel 1990), typically created by episodic or eruptive mass loss (T. J. Moriya et al. 2023). In many cases, it remains uncertain whether the progenitor star was stripped before interacting with a hydrogen-rich CSM—as seen in SN Ia-CSM events—or whether it retained its hydrogen envelope, as indicated by Type IIn SNe exhibiting broad hydrogen lines originating from the ejecta (Y. Sharma et al. 2023). Events such as SN 2002ic (M. Hamuy et al. 2003; N. N. Chugai et al. 2004) and SN 2005gj (G. Aldering et al. 2006) provide some of the first potential evidence for the SN Ia-CSM subclass.

Due to the high levels of CSM interaction that seemingly overpowers other sources such as radioactive ^{56}Ni decay, it is expected that the progenitor system undergoes significant mass loss prior to the time of explosion. Because a high mass-loss rate $\gtrsim 10^{-3}\,M_{\odot}$ yr^{-1} is required for wind breakouts (M. R. Drout et al. 2014; E. O. Ofek et al. 2014a; S. Gezari et al. 2015; E. Waxman & B. Katz 2017), massive stellar models that undergo tumultuous mass-loss changes and have unstable envelopes such as red, yellow, and blue supergiants (RSGs, YSGs, and BSGs), are likely to be possible progenitors (I. Arcavi 2017; N. Smith 2017). There has been direct evidence (e.g., SN 2005gl; A. Gal-Yam et al. 2007; A. Gal-Yam & D. C. Leonard 2009, SN 2009ip; N. Smith et al. 2010b; J. C. Mauerhan et al. 2013) that luminous blue variables (LBVs; N. Smith 2026), which undergo turbulent histories and mass loss in the transition to the Wolf–Rayet phase, are a progenitor type for Type IIn SNe. In addition, about 50% of all Type IIn SNe experience observable "precursor" events within approximately four months before core collapse, releasing significant amounts of mass into the environment (N. Smith et al. 2010b; J. C. Mauerhan et al. 2013; E. O. Ofek et al. 2014b; I. Arcavi 2017; N. L. Strotjohann et al. 2021).

Another leading theoretical mechanism for the formation of CSM around Type IIn SNe is binary interaction (N. Smith & W. D. Arnett 2014; N. Smith 2017). The binary interaction scenario offers several advantages as it can naturally account for asymmetric or nonspherical CSM distributions (N. Smith 2017). However, the wind velocities associated with Roche-lobe overflow in binary systems are typically insufficient to explain the most luminous events, such as SN 2006gy, SN 2006tf, and SN 2010jl (N. Smith 2014, 2017). Recent studies suggest that binary mass transfer can reproduce the observed brightness distribution of most Type IIns (A. Ercolino et al. 2026); though, the most luminous Type IIns likely represent a more complex subset. Regardless, binary interaction may remain a key factor in shaping the geometry, density, and overall distribution of the CSM in both steady-wind and eruptive mass-loss environments (N. Smith 2017).

Due to the diverse progenitor channels and complex interactions with the CSM, Type IIn SNe exhibit the broadest range of absolute brightness among all SN types, spanning over six magnitudes (N. Smith 2017). Type IIn SNe are frequently among the most luminous and superluminous[38] SNe (SLSNe; D. A. Howell 2017), defined as those with peak magnitudes $M_x \leqslant -21$ in any optical band (A. Gal-Yam 2012, 2019). Similar to conventional SNe, SLSNe are classified by hydrogen content: SLSNe-I lack hydrogen in the spectra, and SLSNe-II are hydrogen rich. While the explosion/progenitor systems are still unknown, most SLSNe-II have the time evolving narrow emission lines reminiscent of Type IIn spectra (R. M. Quimby et al. 2018), suggesting they may represent a luminous extension of the Type IIn population, which we will refer to as SLSNe-IIn. Whether SLSNe-IIn are sufficiently distinct from the broader diversity of Type IIn SNe to be considered a separate classification remains under discussion. For clarity, we adopt the superluminous designation to distinguish the more luminous events with which SN 2019vxm is more closely associated.

Some of these more luminous and superluminous Type IIn include SN 2003ma (A. Rest et al. 2011), SN 2006gy (N. Smith et al. 2007; E. O. Ofek et al. 2007; N. Smith et al. 2010a), SN 2006tf (N. Smith et al. 2008), SN 2008am (E. Chatzopoulos et al. 2011), SN 2010jl (N. Smith et al. 2011; E. O. Ofek et al. 2014c, 2019), SN 2015da (N. Smith et al. 2024), and SN 2017hcc (N. Smith & J. E. Andrews 2020; P. Chandra et al. 2022; S. Moran et al. 2023). As the shock traverses the extended CSM structure, SLSNe-IIn can remain bright for years (N. Smith 2017). The complexity of their CSM interactions makes studying Type IIns—particularly the most luminous—productive for understanding star formation and dust production (e.g., M. Shahbandeh et al. 2025).

A key feature of core-collapse SNe, including many Type IIn SNe and SLSNe-IIn, is the emergence of early radiation from the stellar surface following explosion. After a core collapse, the first photons escape from the optically thick stellar surface in a process known as a "shock breakout" (E. Waxman & B. Katz 2017). This occurs when a shock wave, generated deep within the optically thick interior of the progenitor's stellar interior, travels outward and reaches the stellar surface. Upon breakout, a brief but intense flash of X-ray/UV radiation is released, as potentially first seen in A. M. Soderberg et al. (2008), with a duration ranging from a

[38] There is ongoing debate regarding both the definition and the validity of classifying superluminous Type IIn SNe, as they are not clearly distinct from the broader Type IIn population (D. Hiramatsu et al. 2024). Here, we adopt this designation solely to denote their high luminosity, without implying a physically distinct subclass.

few seconds to several hours, depending on the progenitor's size and structure and the shock's energy and geometry (B. Katz et al. 2010; C. D. Matzner et al. 2013; E. Waxman & B. Katz 2017; C. M. Irwin et al. 2021; C. M. Irwin & K. Hotokezaka 2025). As the shock-driven outermost stellar layers expand and cool, ejected by the internal shock, they emit UV/optical radiation, typically lasting several days (E. Chatzopoulos et al. 2012; E. Waxman & B. Katz 2017). This early emission often constitutes the first detectable light from an SN (E. Waxman & B. Katz 2017). Optical counterparts to these events can be regularly detected for Type II SNe (I. Irani et al. 2024), with examples including the high-cadence Kepler observations of the Type IIP SN KSN 2011a/d (P. M. Garnavich et al. 2016) and the rapidly rising Type IIb SN 2016gkg (M. C. Bersten et al. 2018).

In this paper, we analyze the photometric data for SN 2019vxm, a Type IIn SN or superluminous-IIn (SLSN-IIn)—discovered by the ASAS-SN team (C. S. Kochanek et al. 2017) and given the designation ASASSN-19acc (K. Z. Stanek 2019)—and the gamma-ray burst GRB 191117A detected by the Fermi Gamma-ray Burst Monitor (GBM). Many high-cadence surveys including TESS and ATLAS gathered data, giving SN 2019vxm a well-constrained rise and one of the most complete photometric coverages for any Type IIn SN. Spectroscopic analysis of SN 2019vxm will be presented in N. Smith et al. (2026, in preparation).

SN 2019vxm was found at a redshift of $z_{\rm hel} \approx 0.019$, peaking at a nonextinction corrected absolute magnitude of $M_V = -20.12$ mag[39] (D. Tsvetkov et al. 2024) and originates from the host-galaxy SDSS J195828.83+620824.3.

In Section 2 we discuss the photometric data available as well as the processing and reduction. In Section 3, we analyze the photometric lightcurves and data of SN 2019vxm alongside other Type IIn SNe to identify potential similarities and differences. Section 4 presents the search for and interpretation of optical and X-ray shock breakouts, including a coincidence between the Fermi event GRB 191117A and SN 2019vxm. In Section 5 we model the lightcurve of SN 2019vxm and the host and place constraints on its rise parameters. The main conclusions and discussion are given in Section 7.

2. Data and Reduction

2.1. TESS

While the Transiting Exoplanet Survey Satellite (TESS) space telescope mission (G. R. Ricker et al. 2014) was originally designed with the primary purpose of capturing exoplanet transits, the high-cadence data and wide field of view allow for the imaging and discovery of many transient-like (time-domain astronomy) events. TESS has four cameras each with a 24° × 24° field of view (for a total area of 24° × 96°), imaging a *sector* of the sky in a single broadband red filter, TESS-*R*, for ∼27 days[40] (G. R. Ricker et al. 2014).

For the original mission (2018 April –2020 July), each sector was imaged at a cadence of 30 minutes. The high temporal cadence and the relatively long observing strategy provides a unique opportunity for the classification and discovery of many unique transient-like phenomena. TESS has effectively been used to classify, and even discover many time-evolving high-energy astrophysical phenomena such as SNe (M. M. Fausnaugh et al. 2023; Q. Wang et al. 2023, 2024), and gamma-ray burst (GRB) afterglows (M. M. Fausnaugh et al. 2023; R. Jayaraman et al. 2024; H. Roxburgh et al. 2024; D. A. Perley et al. 2025).

While TESS has great temporal resolution, it has relatively poor spatial resolution, where each pixel is approximately 21″ × 21″, with an effective point-spread function (ePSF)[41] with a full width at half maximum (FWHM) typically between 21″ and 42″ (one to two pixels; K. J. Bell & M. E. Higgins 2022). Because of the undersampled ePSF, any PSF photometry can be quite dominated by the individual response/sensitivity of the pixels (K. J. Bell & M. E. Higgins 2022).

The full frame images (FFIs), which are (2048 × 2048) pixels^2 for each of the 16 CCDs that can be accessed through the Barbara A. Mikulski Archive for Space Telescopes (MAST; TESS Team 2022), have undergone "calibration," but no subsequent background subtraction. Removing the scattered light background across the detector is highly nontrivial as it evolves rapidly spatially and temporally. The highly elongated orbit between the Moon and the Earth causes scattered light from both the Earth and the Moon to enter TESS's optical path, requiring further reduction pipelines to analyze objects (R. Ridden-Harper et al. 2021).

For the analysis of SN 2019vxm, we utilize the `TESSreduce`[42] (R. Ridden-Harper et al. 2021) difference-image reduction pipeline, which has been successfully used in various astrophysical transient analyses (e.g., S. Tinyanont et al. 2022; Q. Wang et al. 2023, 2024; H. Roxburgh et al. 2024) and is a major component of `TESSELLATE`,[43] the first large-scale transient detection pipeline for TESS (H. Roxburgh et al. 2025). `TESSreduce` uses the `python` package `calibrimbore`[44] to photometrically calibrate the TESS-*R* filter to the Pan-STARRS1 standardized filters.

The `TESSreduce` package provides a choice between aperture and PSF photometry, where the preferred method is circumstantial. Since neither method is consistently preferred in TESS, we compare both approaches, where the preferred practice should be the method that minimizes the flux scatter and instrumental trends. For our analysis, we find that for SN 2019vxm, PSF photometry is the preferred method as it substantially reduces light contamination from other sources, and therefore, we use the PSF reduction on the TESS difference images.

Approximately midway through a sector, TESS undergoes *downlinking*, where the telescope cannot be used for observations for ∼16 hrs while the data onboard the craft gets sent to Earth. The downlinking creates two distinct regions, each with minor differences in calibration, typically a constant offset correction to the baseline of approximately 0.1 → 5 counts. For exoplanetary science this is dealt with by normalizing all of the lightcurves, but for difference-imaging transients this can be complex. To ensure the baseline for the

[39] Converted to the fiducial spatially flat ΛCDM cosmology with $H_0 = 70$ km s^{-1}Mpc^{-1} and $\Omega_{\rm M0} = 0.3$ that can be assumed throughout the rest of the paper.

[40] Depending on the ecliptic latitude, some targets can appear in multiple sectors consecutively.

[41] While it is not uncommon to refer to the ePSF as the pixel response function (PRF) for TESS, we refer to the PRF as the ePSF to be in line with difference-imaging pipelines and methods across various surveys.

[42] https://github.com/CheerfulUser/TESSreduce

[43] https://github.com/rhoxu/TESSELLATE

[44] https://github.com/CheerfulUser/calibrimbore

two regions is identical we fit a simple broken power law to the rise,

$$f = \Theta(t - t_0) \cdot [a(t - t_0)^n + c], \quad (1)$$

where $\Theta(t - t_0)$ is the Heaviside function acting at the time of first light t_0, a is a flux scaling factor, n is a power-law index, and c is a constant linear vertical shift. The modeled t_0 is relative to the time of first light for the specific instrument, where different telescopes with different sensitivities may infer an earlier t_0. A broken power law is the simplest model that can be used to explain the early rise, as seen in Figure 1. While other work assumes the rise is $\propto t^2$ (A. Nyholm et al. 2020), we consider the high-cadence TESS data and the rise color dependence to constrain n, which provides a qualitatively greater fit than assuming $n = 2$. In the presence of more complex dynamics such as seen in the Type Ia SN 2023bee (Q. Wang et al. 2024), or shock breakouts as seen in Kepler high-cadence Type IIP SN (P. M. Garnavich et al. 2016), more complicated models would have to be employed. We tested a range of t_0 values, selecting the value (and subsequent model) that minimizes the error-weighted χ^2/dof, and applying the baseline corrections to the rise of the supernova. The errors presented for the broken power law come from the covariance from the model fitting added in quadrature with the bootstrap resampling errors from the weighted sample of the other t_0 cuts. We note that the modeled t_0 is relative to the sensitivity of the TESS telescope and it is possible that larger telescopes would find an earlier rise.

To flux calibrate the TESS data, we use ATLAS magnitudes taken about 0.5 days before the first spectra available on the `Transient Name Server` (TNS).[45] We assume that (i) the power-law relation describing the rise remains valid at the epoch of the first spectrum, a few days after the final TESS observation, and (ii) SN 2019vxm does not undergo any significant spectral evolution over a timescale of 0.5 days.

We first extrapolate the best-fit power-law model to the time of the first spectrum to predict the corresponding ATLAS magnitude, adopting a standard zero-point (R. Vanderspek et al. 2018). The difference between this predicted value and the observed ATLAS magnitude defines the magnitude offset between the model TESS flux and the ATLAS measurement. We apply this offset (−0.052 mag) to the ATLAS magnitude.[46]

Using the corrected AB calibrated ATLAS magnitude, we performed synthetic photometry with `pysynphot` (STScI Development Team 2013) and the relevant passbands to derive the expected magnitude for the TESS-*R* band, calculating the zero-point to be zp = 20.57, which is 0.13 mag higher than the prototypical Vega-system zero-point of 20.44—based on the Cousins *I* band[47] commonly adopted in TESS photometry (R. Vanderspek et al. 2018).

2.2. ATLAS

The Asteroid Terrestrial-impact Last Alert System (ATLAS) program is a series of four Schmidt 0.5 m telescopes

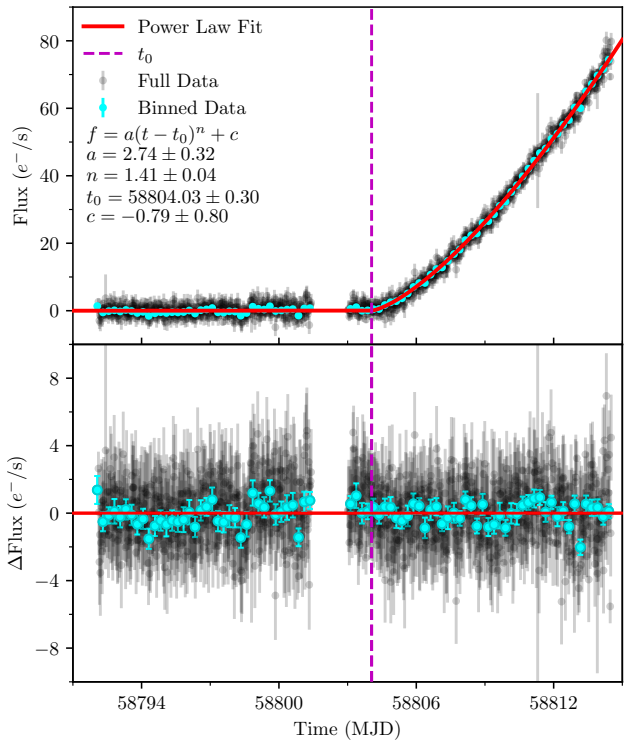

Figure 1. The rise of SN 2019vxm in the native 30 minute cadence and 6 hr bins after adjusting the baseline to follow zero flux. Both plots show the complete rise and the data binned in 6 hr sections. Top: the flux for Sector 18 with a simple broken power-law fit to the rise. We show the value for c despite the baseline correction already having been applied in the figure. Bottom: the residual, $\Delta\text{Flux} = \text{Flux}_{\text{l.c.}} - \text{Flux}_{\text{p.law.}}$, between the lightcurve and the fit power law, to test for significant deviations in the lightcurve.

(two at the time of SN 2019vxm), primarily designed for asteroid and near-Earth-object detection (J. L. Tonry et al. 2018a). Despite the designed purpose, ATLAS has discovered over 4000 SNe and other transients up to ∼19.5 mag (J. L. Tonry et al. 2018a; K. W. Smith et al. 2020). ATLAS primarily uses two filters, *ATLAS-o* (orange) and *ATLAS-c* (cyan),[48] that were originally calibrated using *APASS* (in the south) and Pan-STARRS1 (north of −30° decl.) photometry, but now include Gaia, the Tycho-2 catalog, the Yale Bright Star Catalog, and *SkyMapper* (J. L. Tonry et al. 2018b). *ATLAS-o* and *ATLAS-c* can be approximated using linear combinations of the Pan-STARRS1 *g*, *r*, *i* filters for stellar spectral energy distributions as given by J. L. Tonry et al. (2018a, Equation (2)).

Unlike TESS, which observes a section of the sky continuously, ATLAS is a ground-based program and on a clear night images almost all of the visible sky at four epochs to form quads (J. L. Tonry et al. 2018a). Therefore, the nominal cadence is approximately four times every day in the *o*-band, and less in the *c*-band.

We produce the ATLAS lightcurve using `ATClean`[49] (S. Rest et al. 2025), which is built upon the methods described in J. L. Tonry et al. (2018a) and K. W. Smith et al. (2020) to perform forced PSF photometry on SN 2019vxm. `ATClean` performs multiple forced difference-imaged photometry on the target and at several surrounding noncrowded locations

[45] https://www.wis-tns.org/
[46] While we would not expect the magnitude offset to be identical between the two bands, they are a good approximation over such a small magnitude shift.
[47] https://tess.mit.edu/public/tesstransients/pages/readme.html
[48] ATLAS does have other bands, including a *t*-band (tomato); however, SN 2019vxm was not captured in these bands.
[49] https://github.com/srest2021/atclean

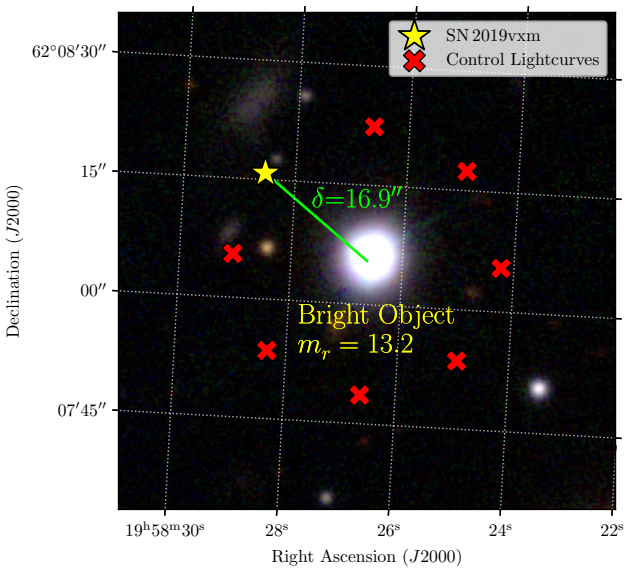

Figure 2. An overlay of SN 2019vxm and the control lightcurve positions used in the `ATClean` reduction on a tricolor (*g*, *r*, *i*) Pan-STARRS1 image, colored using the `AstroColour` package. The control lightcurve positions were chosen relative to the bright source near SN 2019vxm, as that will be the main source of contamination.

without bright sources, as seen in Figure 2, to produce *control lightcurves*. This procedure removes outliers by testing if uniform changes in brightness are detected across the control samples. The control lightcurve positions can be seen in Figure 2.

2.3. Pan-STARRS1

The Pan-STARRS1 survey is one of the most complete and well-calibrated photometric surveys, covering the entire northern sky (decl. $> -30°$) since 2007 (K. C. Chambers et al. 2016). Initially calibrated using synthetic magnitudes and the *Sloan Digital Sky Survey*, it now relies on its own catalog for calibration due to the large data volume (E. A. Magnier et al. 2020). Pan-STARRS1 employs *Iteratively Weighted Least-Squares* photometric techniques to determine the flux of each target following extensive pixel detrending, as outlined in C. Z. Waters et al. (2020), which is applied to the output difference-imaged forced photometry AB magnitude lightcurve (E. A. Magnier et al. 2020). Because SN 2019vxm is in a rarely visited field of the Pan-STARRS1 survey, only a few detected points exist. There is no detection of any excess flux or precursor activity in 98 images taken between MJD 57505 and 58765. These are mostly 45 s *i*-band images, with around 10 *z* or *y*-band 30 second exposures. The 3σ forced limits for the *i*-band images are $i \gtrsim 21.2$.

2.4. ZTF

The Zwicky Transient Facility (ZTF; E. C. Bellm et al. 2019) is a wide-field Northern Hemisphere survey that operates with a cadence of ∼2 days. The survey utilizes two telescopes, a 1.2 m and a 1.5 m, at Palomar Observatory, primarily aimed at detecting transient events such as novae and GRBs with a photometric precision of 8 to 25 mmag (F. J. Masci et al. 2019). The data products for SN 2019vxm were created using the forced photometry service described in F. J. Masci et al. (2023), which computes AB magnitudes using the extensive Pan-STARRS1 catalog as a reference for computing the zero-point of the field.

2.5. Konkoly

The Konkoly Observatory in Hungary houses several telescopes ranging in size from 0.4 m to 1.0 m at Piszkéstető Mountain Station. The data were taken with the 0.8 m Ritchey-Crétien robotic telescope, in Johnson–Cousins *BV* and Sloan *griz* filters. The data were processed with standard `IRAF` routines, using aperture photometry. Measurements were standardized using the Pan-STARRS Data Release 1 (PS1) magnitudes of the stars near the supernova in the field of view (K. C. Chambers et al. 2016). For a more detailed description, we refer to B. Barna et al. (2023); a separate analysis of the Konkoly data, together with the photometry by D. Tsvetkov et al. (2024), will be presented by Lelkes et al. (2026, in preparation).

2.6. Fermi

The Fermi Gamma-Ray Space Telescope conducts an all-sky survey for photons in the energy range of ∼8 keV to ∼300 GeV.[50] The primary instrument, the Fermi Large Area Telescope (W. B. Atwood et al. 2009), has a wide field of view of ∼7880 deg^2, covering about 20% of the sky, and is sensitive to gamma rays in the range of ∼20 MeV to ∼300 GeV (W. B. Atwood et al. 2009).

The secondary instrument, the Gamma-ray Burst Monitor (GBM), observed GRB 191117A, which we associate with SN 2019vxm (see Section 4.2 for details on the associated probability). The GBM is equipped with 12 sodium iodide (NaI) scintillators and two bismuth germanate (BGO) scintillators. The detectors are capable of detecting X-rays and low-energy gamma rays (up to 1 MeV for NaI and 40 MeV for BGO) over the entire sky not occulted by the Earth (C. Meegan et al. 2009; S. Poolakkil et al. 2021). The time-tagged event (TTE) data from the GBM catalog objects (A. von Kienlin et al. 2014; D. Gruber et al. 2014; P. Narayana Bhat et al. 2016; A. von Kienlin et al. 2020) is highly versatile, recording the time and energy of each event with a cadence of 5 μs, often binned for a "cleaner" analysis. With the time and energy information, a conventional lightcurve product can be created, while the energy and timing information can create a forward-folded spectrum from the incoming photons as seen in Figure 3.

To analyze the GBM data, we use the `gdt-fermi`[51] package (A. Goldstein et al. 2023), which is built upon the `gdt-core` structure (A. Goldstein et al. 2024). The Gamma-ray Data Tools (GDT) packages extract data from the NASA High Energy Astrophysics Science Archive Research Center (HEASARC),[52] enabling the time-binning of the data, extraction of energy-integrated flux, and time-integrated energy, for generating the lightcurve and energy spectra. For GRB 191117A, the prompt emission was detected by multiple GBM NaI scintillation detectors (with NaI 6 and NaI 7 being the only two significant events), which were therefore used in

[50] Corresponding to a wavelength range of ($\sim 1.5 \times 10^{-10}$ to $\sim 4 \times 10^{-18}$) m.
[51] https://astro-gdt.readthedocs.io/projects/astro-gdt-fermi/en/latest/index.html
[52] For SN 2019vxm the relevant data can be found at: https://heasarc.gsfc.nasa.gov/FTP/fermi/data/gbm/triggers/2019/bn191117006/.

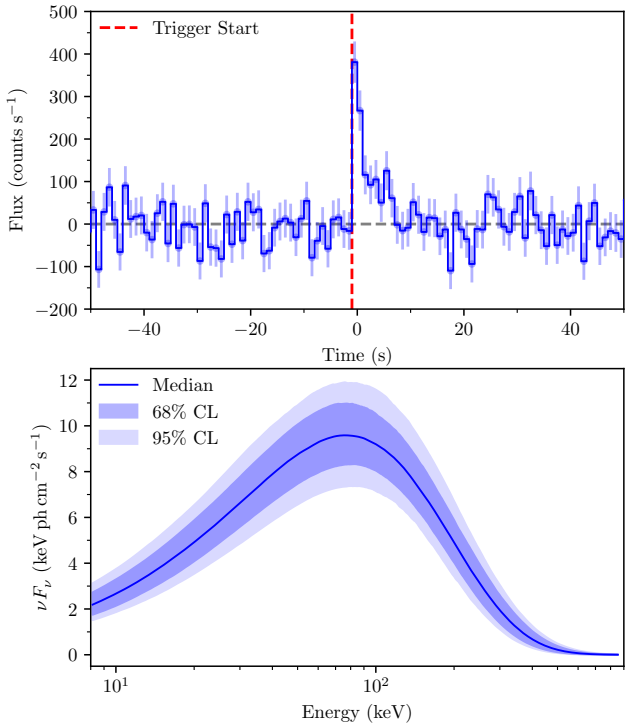

Figure 3. The summed detectors N6 and N7 X-ray/gamma-ray Fermi-GBM data within the energy range 8–900 keV binned in increments of 1 s for the displayed lightcurve and 0.512 s for the spectral analysis. Top: the background subtracted Fermi lightcurve. Bottom: the energy-calibrated and forward-modeled spectrum using a Comptonized model showing the peak energies of the X-ray photons detected at the time of the event. The 68% and 95% confidence regions for the Comptonized model are shown by the shaded regions.

the subsequent analysis. We integrate the energy over 8–900 keV to avoid the lower-energy ranges where the GBM response is poorly calibrated and to avoid the overflow channel in the higher-energy ranges.

We also use the `gdt-fermi` package to fit a line to the time intervals before and after the Fermi signal, in order to create a background subtracted lightcurve and spectra. While higher-order polynomials can be used with `gdt-fermi`, there becomes a risk of overfitting, so we utilize the simplest model for background subtraction.

2.7. Swift

The Swift observatory (N. Gehrels et al. 2004) was primarily commissioned to detect and localize GRBs,[53] and within ∼90 s slew the observatory for X-ray and ultraviolet/optical observations. Swift is unique in that all three of the telescopes are focused on detecting photons at higher-energy levels than the optical wavelengths. It is one of the only space telescopes in operation that can detect both ultraviolet, with the use of the UltraViolet/Optical Telescope (UVOT), and X-rays, with the X-ray Telescope (XRT).

For this analysis, SN 2019vxm has data from both the Swift-UVOT and Swift-XRT telescopes. The Swift-XRT data was taken several days after the Fermi-GRB telescope data. The Swift-XRT data, however, only provided upper bounds on the activity while the Fermi data (Section 2.6) may provide X-rays at the time of first light.

The ultraviolet and bluer optical wavelength ranges help to further constrain SN luminosity around peak brightness. Swift-UVOT has six filters with effective central wavelengths ranging from 2076 to 5412 Å, covering the ultraviolet to visual bands. The Swift-UVOT data were analyzed using the pipeline of the Swift Optical Ultraviolet Supernova Archive (SOUSA; P. J. Brown et al. 2014), including the updated zero-points of A. A. Breeveld et al. (2011) and an aperture corrections based on the average UVOT PSF. These Vega magnitudes were converted to the AB system.

2.8. Gaia

Unlike `TESSreduce` for TESS, ATLAS, Pan-STARRS1, and ZTF, Gaia does not perform difference imaging in the traditional sense, but instead relies on precise astrometric measurements and source detection methods (Gaia Collaboration et al. 2016). Gaia contains multiple filters, but relies on the use of its broadband Gaia-*G* filter for most observations. We convert the Gaia-*G* band from the Vega system to the AB magnitude system.

2.9. LCOGT

We also make use of data from the Las Cumbres Observatory Global Telescope Network as a part of the Global Supernova Project (LCOGT; T. M. Brown et al. 2013), which has a series of 12 different 1 m photometric telescopes across five different continents[54] equipped with the *Sinistro* cameras. The LCOGT images are processed using the `BANZAI` pipeline (C. McCully et al. 2018).

3. Lightcurve Comparison

We compare the lightcurve of SN 2019vxm, shown in Figures 4 and 5, with those of several well-studied Type IIn SNe, as this can tell us a lot about the extent and density of the CSM and the central power source. To enable consistent comparison across different instruments and detection limits, we measure the time required for each event to fade by two magnitudes in a red-like band from peak. Under this definition, SN 2019vxm exhibits a relatively long decay time: it declines by 2 mag in ∼375 days.

In contrast, many Type IIn SNe—such as SN 2003ma (A. Rest et al. 2011), SN 2005gl (A. Gal-Yam et al. 2007; A. Gal-Yam & D. C. Leonard 2009), SN 2005ip (N. Smith et al. 2009; O. D. Fox et al. 2010; S. Katsuda et al. 2014; O. D. Fox et al. 2020; M. Shahbandeh et al. 2025), SN 2006gy (E. O. Ofek et al. 2007; N. Smith et al. 2007), SN 2006tf (N. Smith et al. 2008), and SN 2017hcc (S. Moran et al. 2023) —fade by 2 mag in $\lesssim$200 days. Instead, SN 2019vxm more closely resembles the long-decaying events, which require ∼200 → 500 days to reach the same decline, such as SN 2008am (E. Chatzopoulos et al. 2011), SN 2010jl (N. Smith et al. 2011; E. O. Ofek et al. 2014c, 2019), and SN 2015da (N. Smith et al. 2024). This extended decay time likely reflects a more massive and radially extended CSM.

Many Type IIn SNe have been detected in X-rays, either through targeted observations or a coincidental pointing. In

[53] The highest energy range that *Swift* can detect is hard X-rays; therefore, a significant portion are X-ray bursts (XRBs). For the purposes of this paper, we define XRB to have a peak photon energy below 100 keV.

[54] The photometry data for SN 2019vxm comes from McDonald Observatory in Texas, USA.

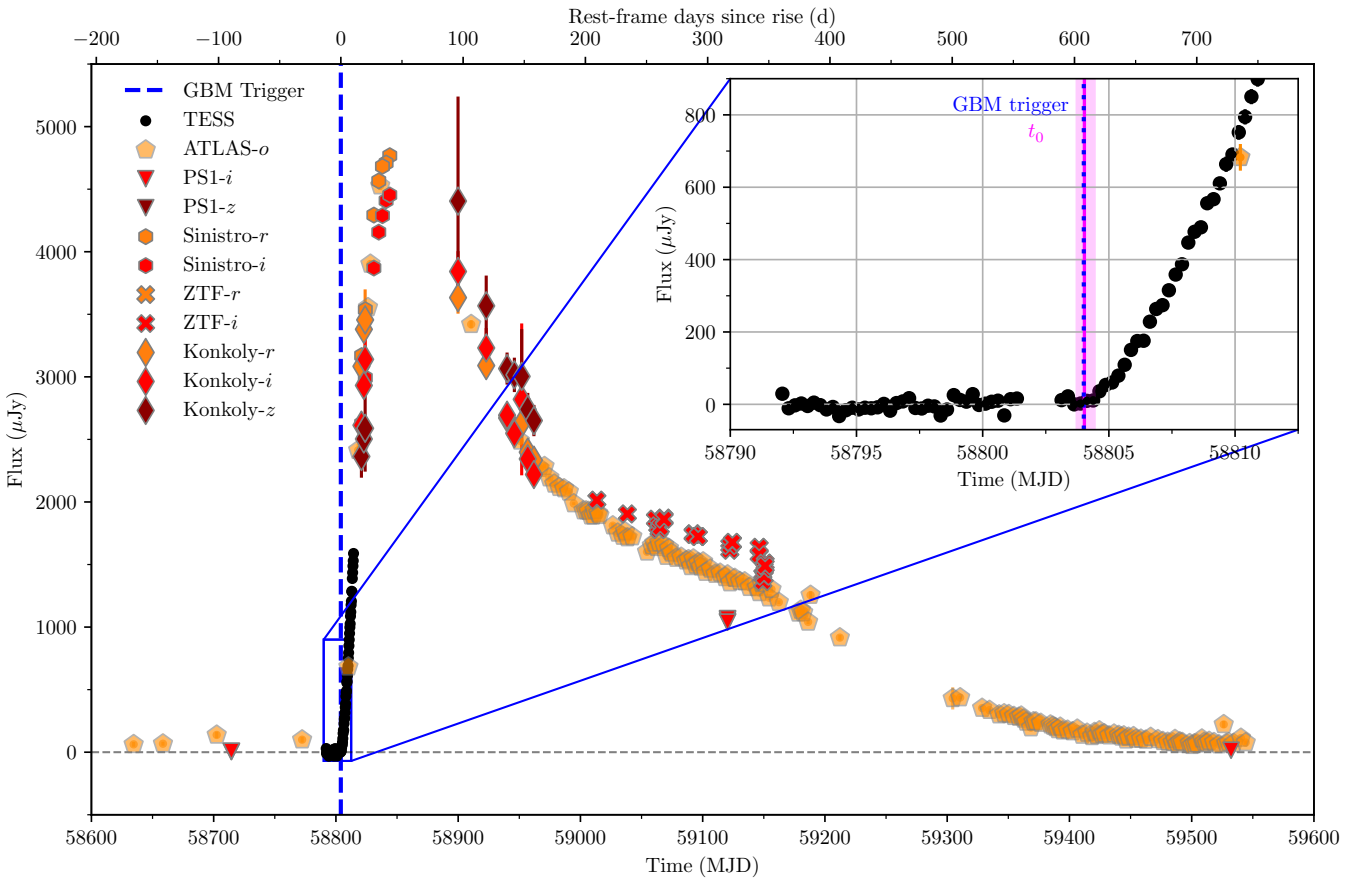

Figure 4. The "redder" filters are plotted in flux-density space to show the GBM trigger alongside the complete rise and decay. The ATLAS data has been binned daily, and the TESS data is binned in groups of 6 hr. We do not take into account band-specific extinction. We note that most of the errorbars are not large enough to be visible. The vertical shaded region in the inset panel refers to the 1σ error around the TESS time of first light.

most cases, however, these detections are limited to relatively "soft" to "harder" X-ray energies, typically between 0.5 and 8 keV. Primarily, this is a consequence of instrumental limitations with most X-ray observatories not being sensitive to energies above ∼8 keV. While the definition of "hard" X-rays is somewhat object- and context-dependent, emission at energies $\gtrsim$10 keV remains largely unexplored for the majority of Type IIn SNe.

While SN 2005ip, SN 2006gy, SN 2010jl, and SN 2017hcc all had X-ray observations spanning from days to years after the explosion trigger (S. Katsuda et al. 2014; E. O. Ofek et al. 2014c; N. Smith et al. 2007, 2017; O. D. Fox et al. 2020; P. Chandra et al. 2022), SN 2019vxm could have one of the first X-rays detected from the trigger of the first light, making the possible detection rather special. The energy spectrum for SN 2019vxm between −2 and 9 s is distinctive, peaking at $E_{\rm peak} = 78.6^{+23.2}_{-19.4}$ keV but extending up to ∼120 keV, depending on the adopted spectral model and binning strategy, higher than most X-ray detections for SNe.[55,56] We adopted a Comptonized model from `gdt-fermi` as that gave the lowest χ^2/dof; however, the peak energy does not vary greatly between different photon flux models. If we simultaneously forward model and constrain a potential higher-energy component using the nondetection from BGO 1 we result in a peak energy of ∼100 keV.

Table 1
The Peak Time and Magnitude Relative to the Time Since Explosion from the TESS-*R* Band Data

Filters[a]	Rise Time (days)	App. Mag.[b] (AB Mag)	Abs. Mag.[b, c] (AB Mag)	δMag
g	$31.0^{+1.5}_{-2.0}$	14.748	−19.836	0.005
S-V	$35.0^{+1.8}_{-1.7}$	14.64	−19.94	0.06
S-B	$35.0^{+1.8}_{-1.7}$	14.78	−19.80	0.05
S-U	$19.8^{+1.6}_{-0.7}$	14.91	−19.67	0.04
S-UVW1	$18.4^{+0.7}_{-0.5}$	15.17	−19.41	0.04

Notes. Minor band-specific offsets in the first light time are considered to be negligible. All magnitudes are not corrected for extinction.
[a] The prefix "*S*-" refers to the Swift-UVOT telescope.
[b] Not corrected for extinction.
[c] Despite not being in the Hubble flow, we adopt a fiducial spatially flat ΛCDM cosmology with $H_0 = 70$ km s^{-1}Mpc^{-1} and $\Omega_{\rm M0} = 0.3$.

The absolute magnitude for SN 2019vxm gathered from D. Tsvetkov et al. (2024), which had good coverage of the peak, is $M_V = -21.41 \pm 0.05$ mag when corrected for extinction, but without *K*-corrections. The extinction correction, $A_V = 1.29 \pm 0.32$, combines the contributions and errors from the host spectral energy distribution (described in Section 5.3); the insterstellar medium and local CSM

[55] It should be noted that the limit for most X-ray telescopes is in the soft X-ray regime, which limits the detectability for hard X-rays/more compact progenitors.
[56] During the lightcurve decay, the X-ray spectrum for SN 2010jl did extend up to ∼50 keV, despite peaking at ∼1 keV, while the other SN events were limited to 8 keV.

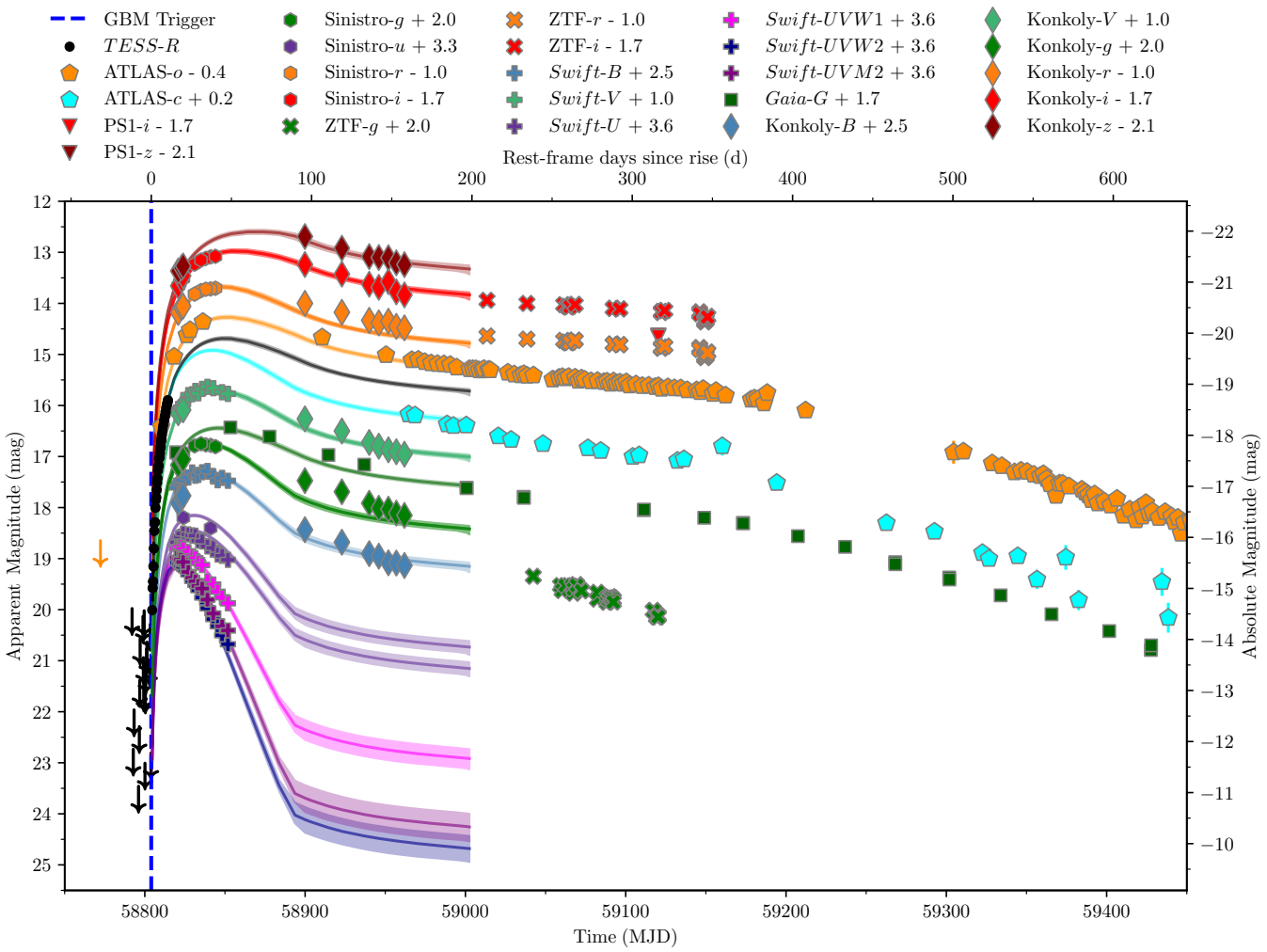

Figure 5. The complete lightcurve in all of the different bands plotted with different magnitude offsets for display purposes. The ATLAS data has been binned daily, and the TESS data is binned in groups of 6 hr. The plotted lines and the respective shaded regions represent the `MOSFiT` lightcurve fitting median and the 5% and 95% confidence regions for each of the respective bands fit within the first 200 days. For further discussion and details for the `MOSFiT` fitting refer to Section 5. For this data we have not corrected for extinction in the magnitudes. We note that most of the errorbars are not large enough to be visible.

environment along the line of sight, inferred by the relation between host hydrogen column density and extinction given by T. Güver & F. Özel (2009) using the `MOSFiT` values; and Milky Way reddening, estimated from the dust map of E. F. Schlafly & D. P. Finkbeiner (2011). The band specific estimates and rise times for the peak magnitude without extinction correction can be found in Table 1. With this correction, SN 2019vxm ranks among the most luminous subcategory of Type IIns alongside SN 2003ma (A. Rest et al. 2011), SN 2006gy (E. O. Ofek et al. 2007; N. Smith et al. 2007), SN 2006tf (N. Smith et al. 2008), SN 2008am (E. Chatzopoulos et al. 2011), SN 2010jl (N. Smith et al. 2011; E. O. Ofek et al. 2014c, 2019), SN 2015da (N. Smith et al. 2024), and SN 2017hcc (N. Smith & J. E. Andrews 2020; P. Chandra et al. 2022; S. Moran et al. 2023).

4. Shock Breakout Analysis

4.1. Optical Precursor and Shock Checks

Type IIn SNe often exhibit precursor events, associated with extreme mass loss (N. Smith 2014; E. O. Ofek et al. 2014b). These outbursts are more prevalent in the period of months prior to the time of explosion, but can take place over years or even centuries (N. Smith et al. 2010b; J. C. Mauerhan et al. 2013; E. O. Ofek et al. 2013, 2014b; C. Bilinski et al. 2015; N. Elias-Rosa et al. 2018).

These mass-ejection events, combined with the assumption that the early lightcurve rise is powered predominantly by shock interaction, suggests potential correlations between the precursor's integrated luminosity and the SN's peak luminosity and rise time (E. O. Ofek et al. 2014b). For SN 2019vxm we attempt to find any evidence for a precursor event, which may persist for several months.

We test the ATLAS and TESS data up to the time of the explosion to search for any precursor-like events. For the ATLAS data we take 150 days prior to the time of first light, while for TESS we only have the month prior.

To find the significance for any precursor or shock breakout events across a range of timescales, we utilize `ATClean` (S. Rest et al. 2025) to minimize artifacts and detect low-level transient emission above zero flux in the ATLAS lightcurve. We can apply a weighted Gaussian rolling sum with different kernel sizes $\sigma_{\rm kernel} = 0.1, 0.2, 0.4, 0.6, 0.8, 1, 2, 3,$ and 5 days, matched to—and thus amplifying—precursor timescales of interest. Our key figure of merit, $\Sigma_{\rm FOM}$, is thus defined as the flux-to-uncertainty ratio convolved with the weighted rolling

Table 2
A Numerical Display of Figure 6 to Display the Magnitude Thresholds for the Optimal Kernel Size and the Rate that Simulated Gaussian Signals Are Recovered at These Thresholds

$\sigma_{\rm sim}$	Best App. Mag. Threshold 50.0%	Best $\sigma_{\rm kernel}$ at 50.0%	Best App. Mag. Threshold 80.0%	$\sigma_{\rm kernel}$ at 80.0%
0.10	18.42	0.10	18.09	0.10
0.20	18.86	0.20	18.50	0.20
0.40	19.20	0.40	18.76	0.20
0.60	19.40	0.40	18.84	0.40
0.80	19.55	0.40	18.98	0.40
1.00	19.61	0.40	19.05	0.40
2.00	19.74	0.40	19.18	0.40
3.00	19.92	3.00	19.26	0.60
5.00	20.19	5.00	19.30	0.60

Gaussian sum. This allows enhancement of faint, extended emission episodes and makes them distinguishable from noise.

To determine whether a detected signal is real, we establish dynamic detection limits $\Sigma_{\rm FOM,limit}$ by analyzing control lightcurves known to contain no astrophysical flux. For each $\sigma_{\rm kernel}$, we adjust the detection limit to allow no more than two control lightcurves with false positives. If any $\Sigma_{\rm FOM}$ exceeded this limit in the SN lightcurve, the signal is flagged as a candidate outburst. This conservative detection limit ensures high purity while maintaining good sensitivity to faint outbursts.

We additionally evaluate the detection algorithm's sensitivity by injecting many synthetic precursor or shock breakout events—both modeled as Gaussian bumps—into the control lightcurves and counting how many were successfully detected. By varying event timescale (i.e., Gaussian $\sigma_{\rm sim}$) and peak apparent magnitude ($m_{\rm peak}$), we can quantify detection efficiency as a function of those parameters. We repeat the process across all $\sigma_{\rm kernel}$. Lastly, we use the resulting efficiency curves to determine the 50% and 80% magnitude detection thresholds for each precursor timescale $\sigma_{\rm sim}$. The detection efficiency is displayed in Table 2 and visualized in Figure 6.

We also exclude several MJD ranges from our analysis if very bright injected simulations do not reach 100% efficiency. First, we exclude gaps between observation seasons, as the lack of measurements makes both real and simulated precursor detection nearly impossible. Second, we add a buffer of one excluded day to our first observation season after observing an edge effect with significantly more nondetections very close to the upcoming season gap.

Ultimately, no statistically significant precursor emission or shock breakouts were detected prior to the ∼5 magnitude rise to peak in the SN 2019vxm lightcurve across the tested timescales in either ATLAS and TESS, allowing us to place stringent constraints on outburst brightness and frequency for the progenitor.

4.2. Localization Probability

To determine the probability for whether SN 2019vxm and the Fermi trigger alert GRB 191117A are the same event or are merely a coincidence, we perform the following tests:

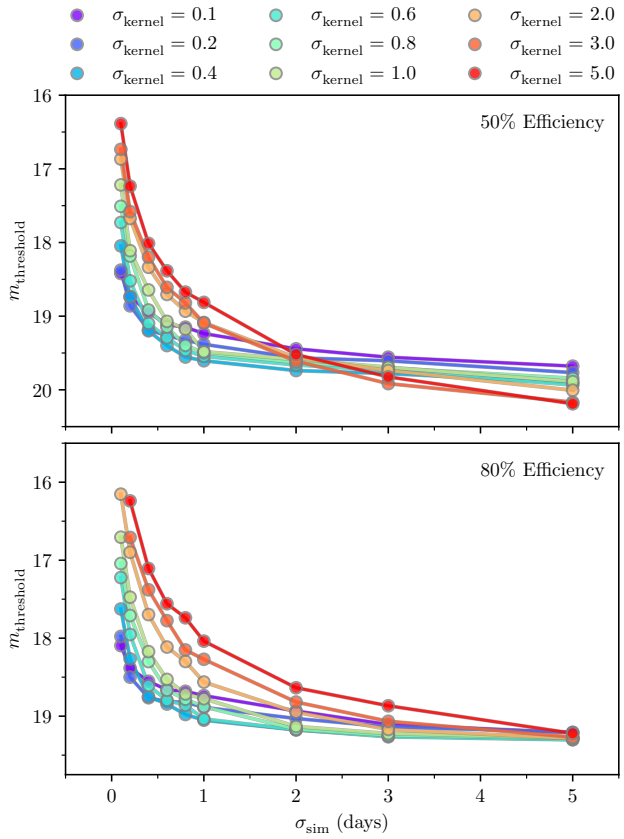

Figure 6. The detection limits for the precursor search in TESS with injected/simulated Gaussian signals, $\sigma_{\rm sim}$ (days), tested against Gaussian kernels of varying widths (days).

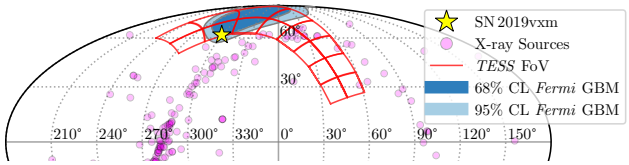

Figure 7. A Northern Hemisphere R.A. and decl. Mollweide-projected skymap showing the position of SN 2019vxm, the asymmetric 68% and 95% confidence level (CL) regions from the probability distribution map, known X-ray binary positions, and an overlay of the TESS pointing for Sector 18. The TESS field covers both 96.7% and 81.9% of the 68% and 95% CL error regions, respectively.

1. Find if there are any other optical triggers within a time frame of ∼3 days using the TESS field.
2. Determine if there are any known X-ray sources, such as X-ray binaries, within 2σ of the GRB trigger.
3. Find the spatial and temporal probability that the two are correlated.

We run the TESSELLATE pipeline (H. Roxburgh et al. 2025) on the sector 18 field of TESS to try and find any transient-like event within a 2σ radius of the reported location of GRB 191117A. The wide FoV of TESS covers 96.7% and 81.9% of the 1σ and 2σ error regions, respectively, for GRB 191117A (refer to Figure 7 for a visual representation). Injection and recovery tests for the TESSELLATE pipeline show ∼50% successful recovery rates up to $m_{\rm TESS} \sim 17$, and no event other than SN 2019vxm was detected. This could mean that either (i) a hypothetical coincident event was not bright enough in the TESS-*R* band, or (ii) the optical component was a prompt emission/evolved

quickly in time, e.g., lasted less than 30 minutes or (iii) was not covered within the TESS field, i.e., outside the observed region. Nevertheless, the fact that SN 2019vxm is the only detected transient within the error region makes it a strong candidate for association with the XRB (see footnote 47 for the definition of XRB in this context).

4.2.1. Spatial Coincidence

In addition to the optical analysis, we compared the spatial position of GRB 191117A with entries in the `XRBcats` X-ray binary catalog[57] (A. Avakyan et al. 2023; M. Neumann et al. 2023) to exclude an association with any known repeating X-ray source. As `XRBcats` lists no known X-ray binary within the 2σ error region of GRB 191117A, this supports the identification of SN 2019vxm as a likely source.

To estimate the spatial probability of two events being colocated, we utilize the `gdt-fermi` package (A. Goldstein et al. 2023) to load the probability localization `HEALPix` map (K. M. Górski et al. 2005). The map yields a lower-bound probability for the spatial discrepancy of $P_{\rm diff,loc}(\boldsymbol{x}) = 2.5\%$. Using the Fermi probability distribution, we evaluate the likelihood of a chance spatial association under the null hypothesis that the sources are unrelated. We load all Fermi-GRB skymaps with `healpy` and, for each GRB, generate 10,000 random sky positions. We then sample the interpolated probability at each position to construct a null (background) distribution. This distribution provides the reference against which we compare the observed sky positions and associated probabilities of GRB 191117A and SN 2019vxm. These simulations yield the probability the two events are the same based on their spatial location alone as $P_{\rm diff,loc}(\boldsymbol{x}) = 0.61\%$.

4.2.2. Temporal Coincidence

When estimating the probability of temporal coincidence, $P_{\rm diff}(t)$, care must be taken in defining the conditioning framework. We considered several formulations for computing the chance coincidence between an SN and an X-ray burst (XRB):

1. for a fixed SN, what is the probability of an XRB happening within a given time frame or vice versa,
2. a symmetric probability formulation upon accounting for a fixed event Y given at least one event Z for both SNe and XRB,
3. the probability of a chance coincidence that these two events occur within a given time frame under null-hypothesis simulations, and
4. what is the probability that an SN and an XRB happen within a certain specified fixed window time frame.

Each approach is valid under specific assumptions, but we focus on those most consistent with our physical scenario and statistical requirements.

Option 1—asymmetric conditioning. This approach assumes one fixed event (e.g., a known SN) and evaluates the likelihood of a second event (e.g., XRB) within a window δt, inherently being asymmetric in formulation. The choice of which rate to use and what assumption to enforce is highly nontrivial. As the observed SNe rate is greater than the observed XRB rate, an argument can be made that the Poisson probability $P(\geqslant 1\ S|\geqslant 1\ X,\ \delta t)_{\rm Poiss.} = 1 - \exp(-\delta t\ R_S)$ should be used, where R_S is the SN rate and δt is the time range of the coincidence window. As the framing of this paper is with respect to the SN itself, conversely, the inverse assumption could be made, $P(\geqslant 1\ X|\geqslant 1\ S)_{\rm Poiss.} = 1 - \exp(-\delta t\ R_X)$; however, both formulations are inherently asymmetric and likely misrepresent the true coincidence.

Option 2—rate symmetric conditioning. To address the asymmetry, we compute a generalized coincidence probability weighted by the respective event rates:

$$P_{\rm diff,\ theory}(t) = \frac{R_{\rm S}P(X|S,\ \delta t) + R_{\rm X}P(S|X,\ \delta t)}{R_{\rm S} + R_{\rm X}}, \tag{2}$$

where $R_{\rm Y}$ is the rate of either XRBs or SNe within a given time frame, and $P(Y|Z,\ \delta t) = P(\geqslant 1\ Y|\ \geqslant 1\ Z,\ \delta t)_{\rm Poiss.}$ is the Poisson probability of an event Y happening given at least one event Z happens within the uncertainty δt.

Option 3—chance-coincidence simulations. The third methodology is most effectively implemented using a brute-force simulation to test the null hypothesis, similar to the approach of A. Moroianu et al. (2023). We generate thousands of synthetic samples of SN and XRB events spanning a 14 year period to estimate the frequency with which the two event types occur within a time interval δt. The empirical probability is defined as

$$P_{\rm diff}(t) = \frac{N^{\rm X}_{\geqslant 1,\ {\rm S}} + N^{\rm S}_{\geqslant 1,\ {\rm X}}}{N_{\rm S} + N_{\rm X}}, \tag{3}$$

where $N^{\rm Y}_{\geqslant 1,\ Z}$ is the number of Y-type events that temporally overlap with at least one Z-type event within δt, and $N_{\rm Y}$ is the total number of Y-type events, drawn from a Poisson distribution. Here, Y and Z represent either SN or XRB events within the simulated time frame, with rates R_S and R_X. We adopt this simulation-based estimate as our fiducial value, as it minimizes assumptions and fully captures the time-domain structure of the data. Notably, the simulated result is consistent with the rate symmetric conditioning probability, confirming agreement between the two methods.

Option 4—fixed-window coincidence. This formulation estimates the probability that the two separate events occur within a predefined time window, as opposed to integrating over all possible time windows δt. This is done computationally by simulating XRB and SNe and counting the overlaps in time. It generally underestimates the true coincidence probability and is considered the least likely choice.

For the SN rate, we adopt the empirical observed rate for core-collapse SN—using the observed fraction of 0.21 of all SN from W. Li et al. (2011) and I. Arcavi (2017) averaged over the last 3 yr reported in the TNS (see footnote 40). Close distance volumetric rates can lead to significant overestimation, as SN brightness and detection efficiency can fall off dramatically beyond $z_{\rm hel.} \sim 0.1$, making redshift cuts both necessary and difficult to implement—particularly given the wide range of possible absolute magnitudes.

For the XRB rate we initially make the conservative overestimate that 50% of all GRBs are actually XRBs and estimate the rate using 14 years of GRB data between 2011 and 2024.[58] We later marginalize the XRB fraction to minimize the impact of this assumption.

[57] http://astro.uni-tuebingen.de/~xrbcat/

[58] https://user-web.icecube.wisc.edu/~grbweb_public/

Table 3
The Probability for the Temporal Association of the XRB and SN 2019vxm

Method	Probability of Coincidence	σ CL
Option 1, XRB rate	11.53%	1.6
Option 1, SN rate	30.66%	1.0
Option 2	15.35%	1.4
Option 3	15.32%	1.4
Option 4	7.36%	1.8

Using $P_{\rm diff.}(\boldsymbol{x}) = 0.61\%$ and $P_{\rm diff.}(t) = 15.3\%$ (from option 3), the probability that the two events are not independent is $P_{\rm same}(\boldsymbol{x}, t) = 1 - P_{\rm diff.}(\boldsymbol{x}) \cdot P_{\rm diff.}(t) = 99.91\%$, corresponding to a 3.3σ confidence level.

We note that many of the values used potentially overestimate the coincidence chance, resulting in a conservative estimate of the probability that the two events are associated.

Instead of using a fixed XRB fraction of total GRBs, we marginalize over the parameter for all options shown in Table 3, giving us $P_{\rm same}(\boldsymbol{x}, t) = 99.91\%$, also corresponding to a 3.3σ confidence level, with 95% and 5% XRB fraction constraints being between 3.2σ and 3.8σ. A more robust temporal coincidence probability calculation would require information about the physical system and the expected time offset between the SN and the XRB to test the null hypothesis; though, this would require great knowledge of the asymmetric 3D CSM structure and the expected time delay. However, despite estimates from Section 5, this is beyond the scope of the paper.

While the probability that the two events are physically associated is high, with only a 0.09% chance of coincidence, the uncertainties—particularly the lack of radial distance information, 3D CSM structure, and reliance on the TESS detection limit—prevent a definitive claim. Therefore, we conclude that the two events are most likely associated.

5. Modeling

Modeling the lightcurve for a Type IIn SNe can reveal important aspects about what the possible progenitor may be, as well as the environment, and other possible physical factors at play. The luminosity and shape profile can tell us about the interaction with the CSM and the mass-loss history for the progenitor/system (N. Smith 2014, 2017; I. Arcavi 2017). Both the luminosity and the duration of the SN during the photospheric phase rely strongly on the diffusion properties of the radiation through the CSM, therefore, they can be used to infer the structural properties of the larger CSM (V. A. Villar et al. 2017). Additionally, further color information can potentially constrain the optical density of the CSM and provide information about the progenitor.

5.1. Model Used and Assumptions

Modeling Type IIn SNe is challenging due to the degeneracies associated with the CSM (refer to Section 6.3 for more details). To address this, we attempt to model SN 2019vxm using CSM-interaction models (E. Chatzopoulos et al. 2012, 2013; V. A. Villar et al. 2017; B. Jiang et al. 2020), which were built upon the earlier pioneering work of W. D. Arnett (1980, 1982). These models simplify the complex dynamics using the following assumptions:

1. The expansion of the ejecta is homologous.[59]
2. The power/heat source is centrally located.
3. The radiation pressure dominates over electron or gas pressure in the equation of state (EoS).
4. There is negligible energy loss due to neutrinos.
5. The mathematical differential equation assumes separability of spatial and temporal behavior.
6. The system is spherically symmetric.
7. The main energy engine is the conversion of kinetic energy to radiation as the shock impacts the dense CSM, while contributions from ^{56}Ni and ^{56}Co radioactive decay are negligible.

Due to the likely asymmetries in the ejecta as discussed in Section 6.2, we adopt the values as illustrative of the progenitor properties to contextualize this event relative to other events, rather than an accurate determination of them.

5.2. Bayesian Modeling

To implement the CSM-interaction models described in Section 5.1, we use the Bayesian inference `python` package `MOSFiT`[60] (J. Guillochon et al. 2018). Specifically, we use the `dynesty` nested sampling package (E. Higson et al. 2019; J. S. Speagle 2020) for the `MOSFiT` models to explore the posterior distribution.

In Bayesian statistics, the *posterior* probability is computed as the ratio of the likelihood and prior to the evidence, given by:

$$\mathcal{P}(\Theta|d,\ M) = \frac{\mathcal{L}(d|\Theta,\ \mathcal{M})\,\mathcal{P}(\Theta|\mathcal{M})}{\mathcal{P}(d|\mathcal{M})}, \tag{4}$$

where Θ are the model parameters, d the data, and $\mathcal{M}$ the model assumed. The likelihood[61] can be written as the $\mathcal{P}(d|\Theta, \mathcal{M})$ term, and $\mathcal{P}(\Theta|\mathcal{M})$ represents the prior π, and $\mathcal{P}(d|\mathcal{M})$ is the evidence $\mathcal{Z}$ of model $\mathcal{M}$.

Since Bayesian sampling relies on prior information, the choice of prior distribution is crucial to obtaining a valid posterior. To be consistent with other notable Type IIn fitting analyses, we adopt the same priors as C. L. Ransome & V. A. Villar (2025) and fix the redshift as $z_{\rm hel.} = 0.019$.

To ensure accurate modeling of the posterior distribution and to take in effect the high number of expected degeneracies in the multidimensional parameter space, we choose a high number of live points, $n_{\rm live} = 1000$, with a tolerance of $d \ln \mathcal{Z} = 10^{-1}$ to match C. L. Ransome & V. A. Villar (2025). We show the posterior parameter distribution in Figure A1, while the lightcurve model can be seen in Figure 5.

5.3. Host Spectral Energy Distribution

We model the host-galaxy spectral energy distribution (SED) using photometry from the Sloan Digital Sky Survey (SDSS), AllWISE, and Pan-STARRS1.[62] The host photometry and stellar population properties are determined through `FrankenBlast` (A. E. Nugent et al. 2026), a rapid tool

[59] The homologous solution assumption has been allowed to relax in the work of E. Chatzopoulos et al. (2012, 2013).
[60] https://github.com/guillochon/MOSFiT
[61] Here, we use a Gaussian likelihood with quadrature noise to account for extended error regions.
[62] Additional infrared data would further constrain the SED and help mitigate parameter degeneracies.

Table 4
Comparing the Galaxy SED of SDSS J195828.83+620824.3 with Other Notable SLSN-Type IIn Using the Data from S. Schulze et al. (2018)

SN Name	Redshift	Host Metallicity $\log_{10}\left(\frac{Z_*}{Z_\odot}\right)$	Host Stellar Mass $\log_{10}\left(\frac{M}{M_\odot}\right)$	Host Age $\log_{10}$yr	Star Formation Rate $\log_{10}$SFR	Specific SFR $\log_{10}$sSFR
SN 2019vxm	0.019	$-0.13^{+0.22}_{-0.26}$	$7.72^{+0.37}_{-0.55}$	$9.75^{+0.15}_{-1.10}$	$-0.89^{+0.27}_{-0.33}$	$-8.63^{+0.57}_{-0.52}$
SN 2003ma[a]	0.289	⋯	$8.91^{+0.13}_{-0.12}$	$7.63^{+0.24}_{-0.29}$	$1.34^{+0.16}_{-0.13}$	$-7.55^{+0.21}_{-0.24}$
SN 2006gy[b]	0.019	⋯	$11.70^{+0.06}_{-0.21}$	$9.91^{+0.10}_{-3.18}$	$-1.12^{+0.08}_{-0.08}$	$-6.78^{+0.12}_{-7.17}$
SN 2006tf[c]	0.074	⋯	$7.54^{+0.47}_{-0.20}$	$8.86^{+0.40}_{-0.35}$	$-1.25^{+0.48}_{-0.37}$	$-8.88^{+0.35}_{-0.29}$
SN 2008am[d]	0.233	⋯	$9.28^{+0.13}_{-0.15}$	$8.57^{+0.33}_{-0.24}$	$0.74^{+0.23}_{-0.24}$	$-8.50^{+0.20}_{-0.35}$
SN 2008fz[e]	0.133	⋯	$6.55^{+0.25}_{-0.28}$	$8.64^{+0.71}_{-0.67}$	$-2.08^{+0.47}_{-0.48}$	$-8.64^{+0.71}_{-0.67}$
SN 2009nm[f]	0.210	⋯	$8.65^{+0.33}_{-0.34}$	$8.95^{+0.62}_{-0.52}$	$-0.60^{+0.65}_{-0.62}$	$-9.20^{+0.79}_{-0.83}$

Notes.
[a] A. Rest et al. (2011).
[b] N. Smith et al. (2007); E. O. Ofek et al. (2007).
[c] N. Smith et al. (2008).
[d] E. Chatzopoulos et al. (2011).
[e] A. J. Drake et al. (2010).
[f] A. J. Drake et al. (2009); E. Christensen et al. (2009).

used for transient host association, host photometry, and SED modeling, and will be compared to the spectra host-galaxy analysis in N. Smith et al. (2026, in preparation).

We classify the host as a dwarf galaxy with a total stellar mass of $M_* = 5.2^{+7.1}_{-3.8} \times 10^7\,M_\odot$ and a stellar metallicity of $\log_{10}(Z_*/Z_\odot) = -0.13^{+0.22}_{-0.26}$. This places the galaxy below both the Small and Large Magellanic Clouds in mass, but with a metallicity comparable to that of the Large Magellanic Cloud (V. Hocdé et al. 2023). The galaxy shows little evidence of AGN activity and exhibits an elevated star formation rate over the past ∼30 Myr, increasing over an order of magnitude from $\sim 10^{-2}$ to $\sim 10^{-1}\,M_\odot\ \mathrm{yr}^{-1}$.

Two environmental trends have been reported for SLSN-IIn host galaxies: (i) they are typically dwarf systems ($M_* \lesssim 10^{10}\,M_\odot$), with massive hosts such as that of SN 2006gy being rare (S. Schulze et al. 2018); and (ii) they display redder $R - K_s$ colors, indicative of older stellar populations and consistent with star-forming galaxies (S. Schulze et al. 2018). The stellar mass of SN 2019vxm is consistent with the dwarf-galaxy regime; however, its $R - K_s$ color cannot be determined due to the absence of NIR observations. We show a comparison of different host properties for SLSN-IIn in Table 4 and Figure 8 based on the data from S. Schulze et al. (2018) and S. Schulze et al. (2021), respectively. No robust conclusions can yet be drawn, given the small sample size and the diversity of host environments. While weak correlations have been found relating the overall luminosity to both low metallicity and a younger stellar age population (T. J. Moriya et al. 2023), it is not necessarily apparent how strongly these impact the total luminosity of the SN. Nonetheless, T. J. Moriya et al. (2023) find that higher mass-loss rates and wind velocities tend to occur in more metal-poor environments, which seems to be consistent with SN 2019vxm. This is, of course, the opposite of what is expected from radiation-driven winds, which should be harder to drive, and have lower $M_\odot$ at low metallicity. In this case it is likely because the CSM is not from radiation-driven winds. It is important to note that metallicity measurements using only photometry are difficult, with stronger constraints coming from spectra. The effect of metallicity explored more in A. E. Nugent et al. (2026) and potentially expanded in A. E. Nugent et al. (2026, in preparation).

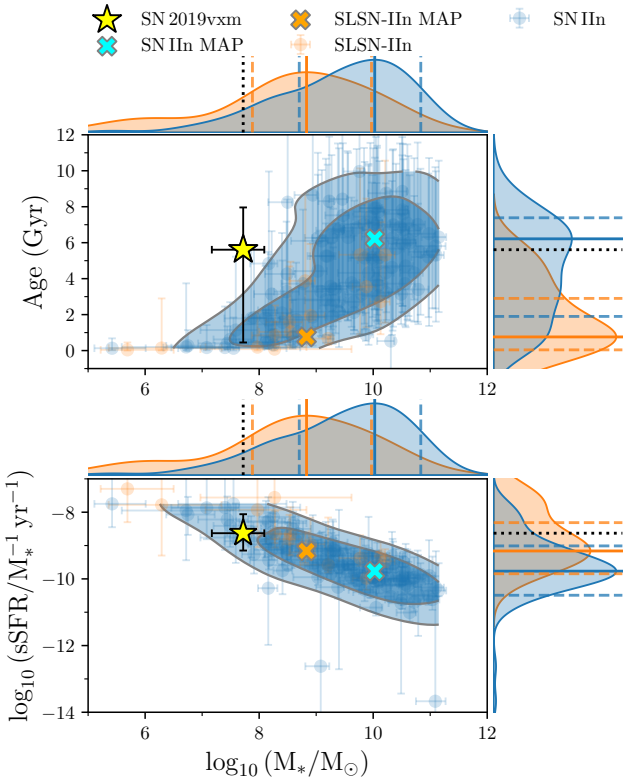

Figure 8. Host SED comparisons between the host of SN 2019vxm and those within the S. Schulze et al. (2021) sample. SN 2019vxm is discrepant with the general Type IIn distribution by 1.8σ for host age and stellar mass and by 1.5σ for host specific SFR and stellar mass. We have marked the Maximum A Posteriori (MAP) values of the posterior on the plot for comparison.

6. Discussion

6.1. Shock Breakout Discussion

For the stellar surface, the higher-energy/stronger emission of X-rays over short timescales (on the order of seconds) are often associated with relativistic surface shock breakouts (R. A. Chevalier & C. M. Irwin 2011, 2012; E. Waxman & B. Katz 2017), while, for slower breakouts, the X-rays are suspected to become dominant for longer at later times.

Typically the shorter timescales and mid- to high-energy X-rays correlate quite strongly with a smaller initial radius of the progenitor (E. Waxman & B. Katz 2017). Indeed, despite the high energy emitted by the explosion of an RSG, significant portions of the radiation are expected to be absorbed by the interstellar medium (ISM), with low–intermediate UV energies produced (E. Waxman & B. Katz 2017). Smaller-radius progenitors, such as BSGs and Wolf–Rayet stars, however, are expected to have shock energies in the medium–high X-ray range (E. Waxman & B. Katz 2017). Both soft and hard X-rays have already been observed for Type IIn SNe, such as SN 2010jl (E. O. Ofek et al. 2014c; P. Chandra et al. 2015); however, these are typically from continued ongoing CSM interaction.

Not only can a shock be formed at the stellar surface, a more luminous shock breakout can be formed more commonly within the dense CSM around a Type IIn SNe progenitor (N. Smith & R. McCray 2007). If the Thomson optical depth, τ, of the CSM is larger than $c/v_{\rm sbo}$, where $v_{\rm sbo}$ is the shock breakout velocity and c is the speed of light, the shock will form within the CSM as opposed to the stellar surface (E. O. Ofek et al. 2014a). Due to the optically thick CSM, and assuming an approximately spherical structure, it is unlikely we will directly observe a stellar surface breakout. In fact, this circumstellar envelope can still significantly change the observable features including spectroscopic line widths, as well as the photon energy and duration for any CSM shock breakout event.

In addition to the breakout itself, another mechanism for UV and X-ray emission in Type IIn SNe arises from ongoing interaction between the ejecta and the dense CSM. Radiatively driven, optically thick winds that formed the CSM can give rise to a collisionless shock once the radiation-mediated shock has passed (E. O. Ofek et al. 2014a; T. J. Moriya et al. 2023). These shocks can produce hard X-rays via inverse Compton scattering and other nonthermal processes. Unlike the shock breakout, which reflects the progenitor's structure, these are later-time emissions, which are more sensitive to the CSM density, geometry, and shock physics. Detectors such as Fermi and Swift among others could possibly detect the X-rays from potential shock breakout events.

6.2. Fermi-GBM Discussion

The Fermi lightcurve precedes the magnitude-limited modeled TESS explosion by 0.61 hr and exhibits a distinct spectral peak at $E_{\rm peak} = 78.6^{+23.2}_{-19.4}$ keV for a simplistic Comptonized photon model. However, depending on the binning and reduction constraints the peak photon energy may be up to 120 keV. The resulting X-ray flash follows the general population in the $E_{\rm peak}$–$E_{\rm iso}$ (Amati) relation (L. Amati 2006; V. Heussaff et al. 2013), indicating that its spectral and energetic properties are consistent with typical X-ray flashes and GRB jets. Such an energy range is consistent with a compact progenitor. Intermediate-mass blue supergiants (BSGs) are expected to produce photons primarily in the 1–10 keV range, while Wolf–Rayet stars typically emit in the 2–50 keV range, sometimes extending to ∼100 keV (E. Waxman & B. Katz 2017).

However, the photon energy of the X-ray flash in the presence of CSM becomes more complex as it must encompass the properties of the shock, and either the density/geometry of the stellar surface or the CSM. The average photon energy produced within the shocked region during a breakout is unlikely to follow a blackbody distribution, and instead can be much larger than the temperature would typically dictate assuming thermal equilibrium (S. Balberg & A. Loeb 2011). The optical depth from a steady wind alone will alter the observed dynamics and properties of the shock breakout (S. Balberg & A. Loeb 2011).

For a standard shock breakout from a barren spherically symmetric stellar surface, the emission timescale is expected to be short, 90% of the integrated counts (T90) for the SN 2019vxm Fermi lightcurve are observed within 7.424 s. Such brief durations generally imply a smaller progenitor radius (M. R. Drout et al. 2014). However, the presence of a CSM can significantly alter the dynamics.

In a spherically symmetric, homogeneous CSM, the effective shock velocity is reduced compared to a direct surface breakout, following the relation $R_{\rm csm} \sim v_{\rm sbo} t_{\rm sbo}$. Consequently, longer observed timescales would generally arise as a result of the lower velocity and the correspondingly larger effective emission radius.

Although the timescale discrepancy could reflect an unrelated source, we discuss three potential distinct physical motivations for this difference, all of which have some pitfalls. An improved understanding of such cases may have to wait for additional examples:

(i) *CSM asymmetry/inhomogeneity.* While shock breakouts are often idealized as isotropic and homogeneous, spectro-polarimetric observations indicate that most, if not all, Type IIn CSM environments exhibit significant asymmetry (C. Bilinski et al. 2024). Spectroscopic line profiles also reveal deviations from spherical symmetry along the line of sight (N. Smith & J. E. Andrews 2020), typically arising from variations in the CSM's density distribution, optical depth, and radial gradients. Unlike in ordinary core-collapse SNe, the first light from Type IIn events often originates from the shock breakout through an optically thick CSM rather than directly from the stellar surface (A. J. Calzavara & C. D. Matzner 2004; N. Smith & R. McCray 2007; N. Smith 2017; E. Waxman & B. Katz 2017).

Intrinsic anisotropies in the explosion itself can further amplify these effects; for example, simulations of RSG progenitors[63] show that the breakout velocity can vary by an order of magnitude across the stellar surface, reflecting differences in breakout radius and the local density structure near the photosphere (J. A. Goldberg et al. 2022a; J. A. Goldberg et al. 2022b). In Type IIn SNe, however, disentangling the geometry of the underlying ejecta from that of the more extended CSM-interaction region requires additional spectroscopic or polarimetric constraints.

For asymmetric CSM configurations, the breakout duration is set by the time required for the shock to traverse the effective CSM surface along the observer's line of sight (S. M. Couch et al. 2011). This differs from the cases of a stellar-surface breakout (S. W. Falk 1978) or a spherically symmetric CSM (E. Waxman & B. Katz 2017; T. Nagao et al. 2020). Consequently, the observed X-ray flash can vary substantially in both duration and luminosity depending on viewing angle, CSM extent, and optical depth.

[63] Other progenitor types likely exhibit similar surface velocity differences due to variations in effective surface density and pressure. For example, 3D simulations of Type IIb progenitors show even greater surface inhomogeneity (J. A. Goldberg et al. 2026).

Table 5
Best-fit MOSFiT Model Parameters for SN 2019vxm, Compared with the Median Values and Parameter Distributions from a Sample of 142 Type IIn SNe (R+V25) Analyzed in C. L. Ransome & V. A. Villar (2025)

Ejecta/SN Params.					
Sample	$M_{\rm ej}$ ($M_\odot$)	$v_{\rm ej}$ (km s^{-1})	$T_{\rm min}$ (K)	$t_{\rm exp}$ (days)	⋯ ⋯
SN 2019vxm	$38.8^{+6.6}_{-6.0}$	6918^{+161}_{-157}	6310^{+147}_{-144}	$-0.86^{+0.08}_{-0.09}$	
C. L. Ransome & V. A. Villar (2025) Sample	$20.1^{+19.0}_{-14.9}$	4721^{+3750}_{-2022}	2587^{+4960}_{-2570}	$-10.4^{+5.7}_{-7.7}$	⋯
Difference	0.94σ	0.59σ	0.75σ	1.67σ	⋯
CSM Params.					
Sample	$M_{\rm CSM}$ $M_\odot$	s ⋯	ρ_0 10^{-12} g cm^{-3}	R_0 AU	n ⋯
SN 2019vxm	$1.48^{+0.14}_{-0.13}$	$1.40^{+0.08}_{-0.08}$	$3.02^{+6.53}_{-1.92}$	$12.3^{+14.0}_{-6.9}$	$7.46^{+0.47}_{-0.29}$
C. L. Ransome & V. A. Villar (2025) Sample	$1.26^{+6.68}_{-0.92}$	$1.37^{+0.67}_{-0.93}$	$6.31^{+0.44}_{-5.81}$	$13.1^{+35.2}_{-9.7}$	$9.44^{+1.79}_{-1.80}$
Difference	0.03σ	0.04σ	0.38σ	0.05σ	1.06σ
Other Params.					
Sample	$N_{\rm H}$ 10^{20} cm^{-3}	σ mag	δ ⋯	ϵ ⋯	⋯ ⋯
SN 2019vxm	$5.75^{+0.70}_{-0.63}$	$0.126^{+0.006}_{-0.008}$	0	0.5	⋯
C. L. Ransome & V. A. Villar (2025) Sample	$0.08^{+6.23}_{-0.08}$	$0.100^{+0.151}_{-0.005}$	0	0.5	⋯
Difference	0.88σ	0.17σ	⋯	⋯	⋯

Note. For each parameter, we report the value for SN 2019vxm, the sample median with uncertainties, and the difference between them in units of σ, accounting for the combined uncertainties. Parameters are grouped into ejecta, CSM, and other model components.

Although asymmetric CSM structures are often invoked to explain extended breakout durations (S. M. Couch et al. 2011), the same structure can theoretically shorten the duration. If the radiation from a shock propagating through an optically thick CSM encounters a locally thinner region with limited angular or physical extent, the effective shock-crossing time across that "edge" of the CSM can be drastically reduced. In such cases, the X-ray flash may last only seconds—set by the geometric light-crossing or local diffusion time—rather than the typical minutes-to-hours expected for a spherical breakout (D. K. Khatami & D. N. Kasen 2024; T. Wasserman & E. Waxman 2026). Thus, a small patch of low optical depth can yield a brighter but much shorter burst, explaining the physical extra brightness (integrated burst energy of $E_{\gamma,\,\rm iso} \approx 3 \times 10^{47}$ erg) and short duration of the Fermi light-curve as photons escape more directly rather than diffusing through extended material (E. Waxman & B. Katz 2017).

As discussed in Section 6.3, the long (∼30 days) rise in the optical and UV lightcurves suggests that the shock breakout occurred within an optically thick CSM extending to roughly 10 au (see Table 5). In such an extended CSM, the initial radiation-driven shock is expected to evolve into a collisionless shock, producing strong X-ray emission over timescales comparable to the optical/UV rise (B. Katz et al. 2010; T. Wasserman et al. 2025). These timescales are far longer than the brief ∼7 s X-ray burst that was observed.

The short burst therefore likely originates from a much more compact region of the CSM, with a characteristic size of only a few tens of $R_\odot$. Emission from such a region would naturally appear short in duration—on the order of seconds—because the light-travel time across it (R / c) limits how long the radiation can be observed. If the surrounding CSM is aspherical, this compact region may be only partially obscured, allowing a direct, transient view of the breakout from one localized patch rather than from the entire extended structure.

It is possible that multiple bound and unbound layers of CSM can create a combined wind and shell-like solution with $s \sim 1.5$ (D. Tsuna et al. 2021), which is within 2σ constraints of the modeled density profile exponent, s, from Section 6.3. The shock breakout diffusion timescale as the forward shock propagates through multiple layers of CSM could potentially produce a shorter diffusion timescale. The difference in the CSM thickness and optical density between the bound and more compact inner regions to the outer layers may effect the observed timescale and observed flux density.

(ii) *"Choked" jet*. A failed or "choked" jet could have developed, quenched by the optically thick stellar envelope or less likely the dense CSM (T. Piran et al. 2019; A. Zegarelli et al. 2024). This scenario produces a mildly relativistic shock with a broad opening angle upon interaction with the CSM, capable of potentially reproducing the observed photon energies, the received flux density, and the burst duration (T. Piran et al. 2019). However, one should always be cautious when interpreting any event as a jet, as geometrical degeneracies often allow jet models to fit the data even if it is not physically motivated. A shocked cocoon of a collapsar-driven jet choked in an extended CSM has been proposed as the solution for other X-ray flashes such as the Type Ib/c-BL, SN 2025 kg (G. P. Srinivasaragavan et al. 2025); however, this event had a longer duration and a less dense CSM than SN 2019vxm, making them difficult to directly compare.

While such an interpretation remains plausible, most of the choked-jet theory has been developed for core-collapse SNe without considering CSM interaction (T. Piran et al. 2019; A. Zegarelli et al. 2024), and is only addressed in a few papers (e.g., P. C. Duffell & A. Y. Q. Ho 2020; G. P. Srinivasaragavan et al. 2025), so further work will have to be done in understanding how the complexities of the environment/geometry has an impact on the photon energy spectrum and the duration.

Another caution, if the jet is "choked," it is unlikely to produce the observed prompt emission. The high-quality TESS data suggest a weak or absent afterglow. While an afterglow without prompt emission is possible, generating prompt emission without an afterglow is difficult, as jet–medium interaction inevitably produces synchrotron radiation.

(iii) *Longer-duration event*. A third possible explanation is that the event lasted longer than observed, with only the peak detected because the low flux-density fell below the background noise. In this scenario, the total time-integrated energy from the interaction would be higher, and the true timescale would be more naturally explained by diffusion through a CSM. While this scenario cannot be dismissed, the sharp peak in the Fermi lightcurve would still likely require both asymmetries in the CSM distribution and a clear line-of-sight/specialized observing angle to reproduce the observed features when compared to the softer peak in the two-dimensional Swift-XRT simulations of S. M. Couch et al. (2011).

We are led to conclude that, so far, an inhomogeneous/aspherical CSM is likely the most physically plausible explanation. However, all three interpretations face theoretical challenges, which would require further observations or models.

6.3. Lightcurve Modeling Discussion

The `MOSFiT` analysis presented by C. L. Ransome & V. A. Villar (2025) involves 11 free parameters constrained by fitting, along with two fixed parameters. We compare the distribution of 142 Type IIn SNe from that study to the best-fit model parameters for SN 2019vxm, categorized into ejecta, CSM, and other components, as listed in Table 5, including their σ-level tensions.

The ejecta-related parameters in the `MOSFiT` CSM-interaction model include the ejected mass, $M_{\rm ej}$; the characteristic velocity dispersion of the ejecta, $v_{\rm ej}$; the minimum temperature, $T_{\rm min}$, which reflects the model assumption that the photospheric radius expands until this temperature is reached before receding; and the explosion time, $t_{\rm exp}$, relative to the first observation provided, which is 0.26 days before the first light is seen in TESS.

CSM parameters include the CSM mass ($M_{\rm CSM}$); the density profile exponent, s, where $\rho_{\rm CSM} \propto R^{-s}$ and R is the CSM radius; the density at the inner CSM radius (ρ_0); and the n-index, which characterizes the geometric properties of the SN ejecta density profile.

Additional or fixed parameters include the host-galaxy hydrogen column density, $N_{\rm H}$; a white noise parameter, σ, accounting for systematic uncertainties; the outer ejecta density index, $\delta = 0$, following C. L. Ransome & V. A. Villar (2025); and the energy conversion efficiency, $\epsilon = 0.5$, for transforming kinetic energy into radiation during CSM interaction. A large hydrogen column depth could help explain the hardness ratio of the potentially related X-ray spectra as a the host galaxy will have greater absorption of lower-energy X-ray photons (S. M. Couch et al. 2011).

The `MOSFiT` lightcurve parameters infer a compact progenitor. The ejecta profile parameter, $n = 7 \rightarrow 10$ may refer to LBV- or WR-like progenitors as opposed to RSG-like progenitors, which are often fixed at $n = 12$ (S. A. Colgate & C. McKee 1969; C. D. Matzner & C. F. McKee 1999; D. Kasen 2010; R. A. Chevalier & C. M. Irwin 2011; T. J. Moriya et al. 2013; C. L. Ransome & V. A. Villar 2025). When coupled with the large total mass of the system $M_{\rm tot} = M_{\rm ej} + M_{\rm CSM} = 40.3^{+6.7}_{-6.2}\,M_{\odot}$, the high $T_{\rm min}$, provides further evidence for a BSG/LBV-like progenitor. The stated total mass of the system does not include any prior mass loss by winds throughout the star's life during evolution, so the initial mass of the progenitor must have been even higher. The high ejecta mass and velocity produce an energetic explosion with approximately an order of magnitude more energy than typical core-collapse SN (e.g., M. Hamuy 2003), with $E_{\rm KE} = \frac{3}{10} M_{\rm ej} v_{\rm ej}^2 = (1.10^{+0.19}_{-0.18}) \times 10^{52}$ erg. This high mass budget and high explosion energy of $\sim 10^{52}$ erg is reminiscent of some other long-lasting SLSNe IIn like SN 2003ma (A. Rest et al. 2011) and SN 2015da (N. Smith et al. 2024).

The CSM density profile exponent, s (some analyses such as T. J. Moriya et al. 2013 refer to this parameter as w), is commonly fixed in many analyses to either $s = 0$, representing the CSM as a dense optically thick shell, or $s = 2$ representing a steady-wind like CSM distribution. Our best-fit value, $s = 1.40^{+0.08}_{-0.08}$, has over a 5σ tension with either the dense-shell or the steady-wind scenario. Physically, the intermediate slope may reflect a complex mass-loss history involving multiple eruptive episodes superimposed on a steady wind, resulting in a structured CSM with underlying "clumpy," dense shells, which may result in the CSM distribution being inhomogeneous and asymmetric, or more generally, a time-variable mass-loss rate.

The assumption of spherical symmetry in `MOSFiT` likely affects the inferred modeled parameters versus the "true" set of parameters (A. Ercolino et al. 2026); due to the complex dynamics observed (see N. Smith et al. 2026, in preparation, for a more detailed analysis of the CSM dynamics) it is likely the environment is asymmetrically layered in both depth and density. As noted by A. Suzuki et al. (2019), various effects such as radiation hydrodynamics, Rayleigh–Taylor instabilities, Kelvin–Helmholtz instabilities, and Vishniac instabilities (E. T. Vishniac 1983) along the effective ejecta-CSM surface will likely create deviations from the spherical symmetric models used, even when the distribution of both the ejecta and CSM are mostly spherical. However, the 200 days cut can affect observations for Type IIn SNe that rebrighten (e.g., E. O. Ofek et al. 2014b; N. Smith et al. 2009, 2017), likely due to the ejecta interacting with multiple effective dense CSM layers or "clumps" (D. K. Khatami & D. N. Kasen 2024). While recent work has been done in modeling these features by adding other effects such as a "breakout" parameter (D. K. Khatami & D. N. Kasen 2024), the simple case of the CSM-interaction model in the `MOSFiT` model cannot account for such features, so complex lightcurve components that likely come from CSM layers are not reflected in the inferred parameters.

With asymmetric geometries, different regions/zones can be viewed simultaneously with different characteristic velocities (N. Smith 2017). At this level of complexity, the viewing angle and evolutionary stage at which the SN is observed play key roles in determining the luminous features seen in the lightcurve. We typically associate a highly nonspherical geometry with binary interaction, where the CSM has been "deflected" by another body, or where the mass loss is driven primarily by the binary interaction, as in an equatorially concentrated outflow made by Roche-lobe overflow.

Another consideration is that SN 2019vxm is classified as an SLSN-IIn rather than a typical Type IIn SN, which, while sharing the same general features as Type IIn SNe, may affect the inferred parameter values (C. L. Ransome & V. A. Villar 2025). For SLSN-IIn events, MOSFiT's CSM-interaction models can overestimate the CSM mass required to sustain long-duration lightcurves (A. Suzuki et al. 2021; C. L. Ransome & V. A. Villar 2025) in the absence of a potential central engine input. To mitigate this, we restrict our model fitting to within 200 days of the first observation, ensuring the data encompasses the entire rise and a portion of the decline to understand the fall time.

C. L. Ransome & V. A. Villar (2025) compared the simplified CSM-interaction model in MOSFiT to the numerical simulations of L. Dessart et al. (2015) and found reasonable agreement in the inferred CSM masses. In our case, the model yields a physically plausible value of $M_{\rm CSM} = 1.48^{+0.14}_{-0.13}\ M_{\odot}$.

7. Conclusion

In this work, we present a multisurvey photometric analysis of the Type IIn SNe SN 2019vxm, incorporating data from TESS, ATLAS, Pan-STARRS1, ZTF, Fermi, Swift, Gaia, and the LCOGT network. We model the high-cadence TESS rise, the first 200 days of the lightcurve using MOSFiT (following C. L. Ransome & V. A. Villar 2025), and the spectral energy distribution of the host galaxy, SDSS J195828.83+620824.3.

The early TESS lightcurve is well described by a broken power law with an index of $n = 1.41 \pm 0.04$, significantly ($>10\sigma$) shallower than the canonical $\propto t^2$ rise typically assumed for early-time SNe emission. From this fit, we infer a time of first light, t_0, and find that the MOSFiT-derived explosion time precedes the TESS rise by 0.26 day, providing a strong temporal constraint and possible insight into the upper range of the shock breakout velocity distribution.

We assess the combined spatial and temporal coincidence likelihood between SN 2019vxm and the X-ray transient GRB 191117A, finding a 0.09% spatial-temporal chance-coincidence probability, corresponding to a 3.3σ confidence that the events are associated. The brief duration of the X-ray event (on the order of seconds) potentially suggests interaction with a dense, possibly asymmetric CSM, the presence of a weak or "choked" jet, or a longer and fainter XRB event than observed. However, each consideration has issues that require further investigation.

The inferred CSM density exponent, $s = 1.40^{+0.08}_{-0.08}$, indicates a steady pre-SN mass-loss history coupled to periods of eruptive or turbulent outflow, producing an inhomogeneous, clumpy CSM structure. Such an asymmetry may account for both the observed XRB lightcurve duration and the NIR–UV lightcurve properties.

Assuming SN 2019vxm and GRB 191117A are physically associated, the peak photon energy of $E_{\rm peak} = 78.6^{+23.2}_{-19.4}$ keV would typically indicate a more compact progenitor such as an LBV or WR star. However, in the presence of CSM, inverse Comptonization and other effects could increase the average photon energy, and lower-energy X-ray photons may get absorbed by the high hydrogen column density, $N_{\rm H}$, modeled in MOSFiT. More strong evidence of SN 2019vxm having a compact progenitor comes from the MOSFiT best-fit parameter for the geometric SN ejecta density, $n = 7.46^{+0.47}_{-0.29}$, consistent with progenitors in the LBV–WR regime ($n \sim 7$) and marginally extending to BSG-like structures ($n \sim 7$–10). The total SN ejecta + CSM system mass, $M_{\rm tot} = 40.3^{+6.7}_{-6.2}\ M_{\odot}$, provides corroborating evidence that SN 2019vxm has a compact progenitor; considering mass lost by winds during evolution, the initial mass would likely be well above 40 $M_{\odot}$, whereas no known RSG progenitors are this massive. This is just within the upper range for compact progenitors, reinforcing the conclusion that SN 2019vxm originated from a massive, compact star embedded in a structured, asymmetric CSM.

If the association with GRB 191117A is real, SN 2019vxm represents one of the few known cases where a superluminous Type IIn has been associated with an X-ray burst at shock breakout. The high-cadence data from TESS alongside the Fermi X-ray burst offers an unprecedented window into the onset of core collapse and shock breakout in a structured CSM.

Acknowledgments

We would like to thank the anonymous reviewer for the helpful feedback and notes to improve the quality of the research. We greatly appreciate the help of Jan Eldridge for help with initial interpretation and early modeling. We also want to acknowledge the engaging discussions with Ryan J. Foley, Ore Gottlieb, Gautham Narayan, Justin Pierel, Tyler Pritchard, Melissa Shahbandeh, and Louis-Gregory Strolger that helped frame aspects of the analysis and provided stimulating discussions. We acknowledge access to the few Pan-STARRS data points from the Pan-STARRS NEO survey data.

We would also like to thank Rachel Hamburg and Eric Burns for reaching out with improvements for the Fermi analysis while under review; their help and advice strengthened the final results and analysis.

Z.G.L., R.R.H., C.M., and P.M. are supported by the Marsden Fund administered by the Royal Society of New Zealand, Te Apārangi under grants M1255 and M1271. Z.G.L. would like to acknowledge the support of the School of Physical and Chemical Sciences Travel Grant, which contributed to the success of this research. R.R.H. is also supported by the Rutherford Foundation Postdoctoral Fellowship RFT-UOC2203-PD. H.R. is supported by an Australian Government Research Training Program (RTP) Scholarship. Q.W. is supported by the Sagol Weizmann-MIT Bridge Program. S.J.S. acknowledge funding from STFC Grant ST/Y001605/1, a Royal Society Research Professorship and the Hintze Family Charitable Foundation. The Flatiron Institute is supported by the Simons Foundation. K.L. and M.L. were supported by the "SeismoLab" KKP-137523 Élvonal grant of the Hungarian Research, Development and Innovation Office (NKFIH), and by the LP2025-14/2025 Lendület grant of the Hungarian Academy of Sciences. K.L. is thankful for the financial support provided by the undergraduate research assistant program of Konkoly Observatory.

This work was partially supported by NASA ADAP grant 80NSSC22K0494.

The material is based upon work supported by NASA under award number 80GSFC24M0006.

This paper includes data collected with the TESS mission, obtained from the MAST data archive at the Space Telescope Science Institute (STScI). Funding for the TESS mission is provided by the NASA Explorer Program. STScI is operated

by the Association of Universities for Research in Astronomy, Inc., under NASA contract NAS 5–26555.

This work has made use of data from the Asteroid Terrestrial-impact Last Alert System (ATLAS) project. The Asteroid Terrestrial-impact Last Alert System (ATLAS) project is primarily funded to search for near-Earth asteroids through NASA grants NN12AR55G, 80NSSC18K0284, and 80NSSC18K1575; byproducts of the NEO search include images and catalogs from the survey area. This work was partially funded by Kepler/K2 grant J1944/80NSSC19K0112 and HST GO-15889, and STFC grants ST/T000198/1 and ST/S006109/1. The ATLAS science products have been made possible through the contributions of the University of Hawaii Institute for Astronomy, the Queen's University Belfast, the Space Telescope Science Institute, the South African Astronomical Observatory, and The Millennium Institute of Astrophysics (MAS), Chile.

The Pan-STARRS1 Surveys (PS1) and the PS1 public science archive have been made possible through contributions by the Institute for Astronomy, the University of Hawaii, the Pan-STARRS Project Office, the Max-Planck Society and its participating institutes, the Max Planck Institute for Astronomy, Heidelberg and the Max Planck Institute for Extraterrestrial Physics, Garching, The Johns Hopkins University, Durham University, the University of Edinburgh, the Queen's University Belfast, the Harvard-Smithsonian Center for Astrophysics, the Las Cumbres Observatory Global Telescope Network Incorporated, the National Central University of Taiwan, the Space Telescope Science Institute, the National Aeronautics and Space Administration under grant No. NNX08AR22G issued through the Planetary Science Division of the NASA Science Mission Directorate, the National Science Foundation Grant No. AST–1238877, the University of Maryland, Eotvos Lorand University (ELTE), the Los Alamos National Laboratory, and the Gordon and Betty Moore Foundation. Pan-STARRS is now primarily funded to search for near-Earth asteroids through NASA grants NNX08AR22G and NNX14AM74G. The Pan-STARRS science products for LIGO–Virgo–KAGRA follow-up are made possible through the contributions of the University of Hawaii's Institute for Astronomy and Queen's University Belfast and the University of Oxford.

This work is based on observations obtained with the Samuel Oschin Telescope 48 inch and the 60 inch Telescope at the Palomar Observatory as part of the Zwicky Transient Facility project. ZTF is supported by the National Science Foundation under grants No. AST-1440341 and AST-2034437 and a collaboration including current partners Caltech, IPAC, the Oskar Klein Center at Stockholm University, the University of Maryland, University of California, Berkeley, the University of Wisconsin at Milwaukee, University of Warwick, Ruhr University, Cornell University, Northwestern University and Drexel University. Operations are conducted by COO, IPAC, and UW.

The operation of the Konkoly RC80 telescope was supported by the GINOP 2.3.2-15-2016-00033 project of the National Research, Development and Innovation Office (NKFIH), Hungary, based on funding from the European Union.

This research is based on observations made with the Neil Gehrels Swift Observatory, obtained from the MAST data archive at the Space Telescope Science Institute, which is operated by the Association of Universities for Research in Astronomy, Inc., under NASA contract NAS 5–26555.

This research has made use of data and/or software provided by the High Energy Astrophysics Science Archive Research Center (HEASARC), which is a service of the Astrophysics Science Division at NASA/GSFC.

The Fermi Gamma-ray Data Tools are partially funded through the NASA ADAP Grant 80NSSC21K0651 and the NASA SMD Open Source Tools, Frameworks, and Libraries Grant 80NSSC22K1741.

We acknowledge ESA Gaia, DPAC and the Photometric Science Alerts Team (http://gsaweb.ast.cam.ac.uk/alerts).

This work makes use of observations made with the Sinistro instrumentation at McDonald Observatory, operated by the Las Cumbres Observatory network.

Data Availability

All of the data and codes are made public and available at doi:10.5281/zenodo.19560492 and https://github.com/ZacharyLane1204/SN2019vxm.

Software: `AstroColour` (Z. G. Lane 2025), `ATClean` (S. Rest et al. 2025), `dynesty` (E. Higson et al. 2019; J. S. Speagle 2020), `FrankenBlast` (A. E. Nugent et al. 2026), `gdt-fermi` (A. Goldstein et al. 2023), `MOSFiT` (J. Guillochon et al. 2018), `pysynphot` (STScI Development Team 2013), `TESSELLATE` (H. Roxburgh et al. 2025), `TESSreduce` (R. Ridden-Harper et al. 2021), `astropy` (Astropy Collaboration et al. 2013, 2018, 2022), `astroquery` (A. Ginsburg et al. 2019), `healpy` (K. M. Górski et al. 2005; A. Zonca et al. 2019), `matplotlib` (J. D. Hunter 2007), `numpy` (C. R. Harris et al. 2020), `pandas` (W. McKinney 2010), `scipy` (P. Virtanen et al. 2020).

Appendix
`MOSFiT` Corner Plot

We show the corner plot (as seen by Figure A1) following from the `MOSFiT` fit described in Section 5.2.

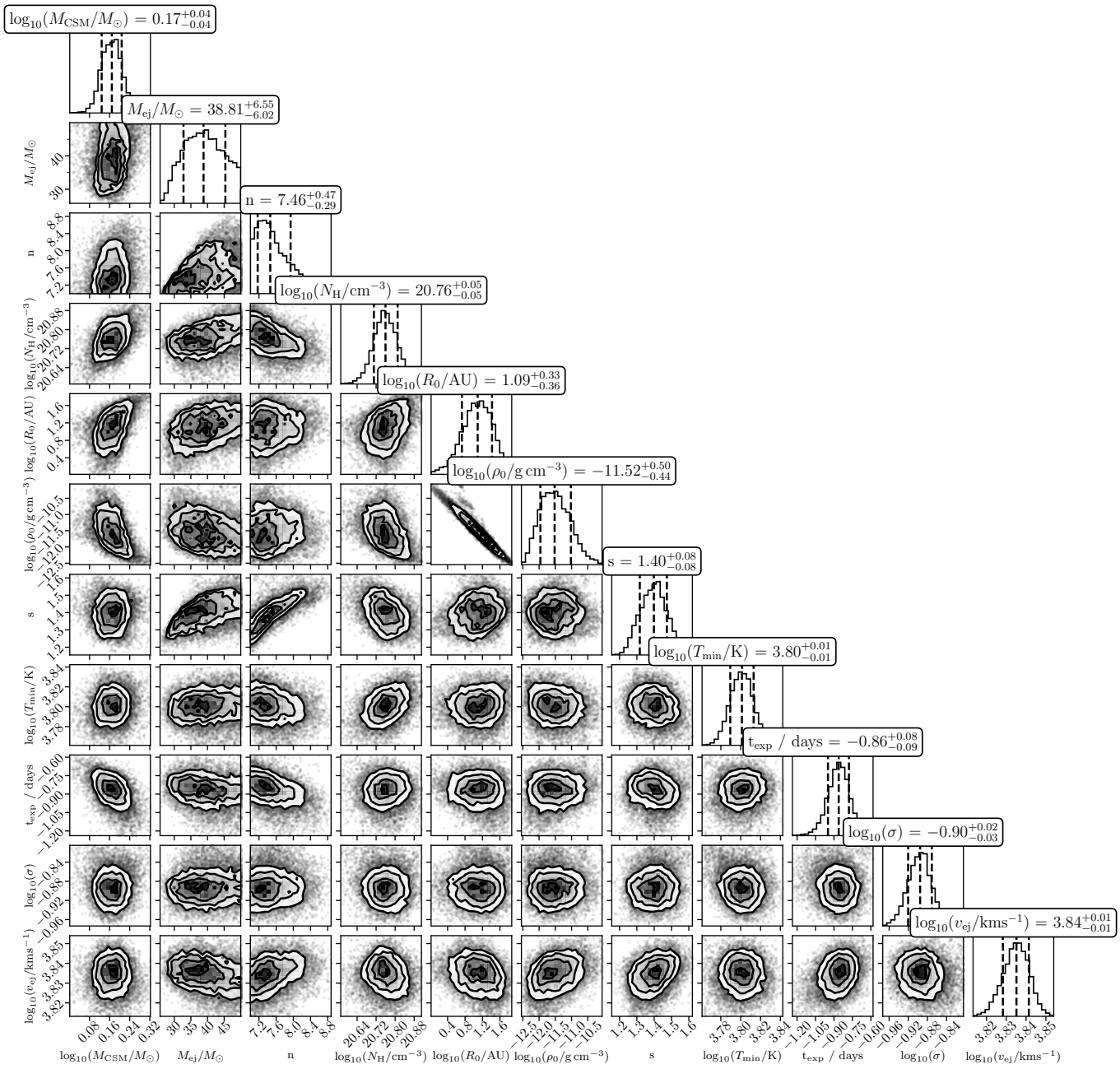

Figure A1. The corner plot for the CSM-interaction `MOSFiT` lightcurve parameters showing their posterior distribution for SN 2019vxm. The diagonal panels show the marginalized probability distributions for each parameter, while the off-diagonal panels illustrate their covariances and parameter degeneracies. We have marked the weighted median as well as the 16% and 84% quantiles of the posterior distribution with dashed lines.

ORCID iDs

Zachary G. Lane https://orcid.org/0009-0003-8380-4003
Ryan Ridden-Harper https://orcid.org/0000-0003-1724-2885
Sofia Rest https://orcid.org/0000-0002-3825-0553
Armin Rest https://orcid.org/0000-0002-4410-5387
Conor L. Ransome https://orcid.org/0000-0003-4175-4960
Qinan Wang https://orcid.org/0000-0001-5233-6989
Clarinda Montilla https://orcid.org/0009-0008-4935-069X
Micaela Steed https://orcid.org/0009-0008-8490-0693
Igor Andreoni https://orcid.org/0000-0002-8977-1498
Patrick Armstrong https://orcid.org/0000-0003-1997-3649
Peter J. Brown https://orcid.org/0000-0001-6272-5507
Jeffrey Cooke https://orcid.org/0000-0001-5703-2108
David A. Coulter https://orcid.org/0000-0003-4263-2228
Ori Fox https://orcid.org/0000-0003-2238-1572
James Freeburn https://orcid.org/0009-0006-7990-0547
Marco Galoppo https://orcid.org/0000-0003-2783-3603
Avishay Gal-Yam https://orcid.org/0000-0002-3653-5598
Jared A. Goldberg https://orcid.org/0000-0003-1012-3031
Christopher Harvey-Hawes https://orcid.org/0009-0002-6751-2695
Daichi Hiramatsu https://orcid.org/0000-0002-1125-9187
Rebekah Hounsell https://orcid.org/0000-0002-0476-4206
D. Andrew Howell https://orcid.org/0000-0003-4253-656X
Brayden Leicester https://orcid.org/0009-0008-6765-5171
Klára Lelkes https://orcid.org/0009-0007-3760-515X
Itai Linial https://orcid.org/0000-0002-8304-1988

Jaime Luisi https://orcid.org/0009-0000-0251-2892
Curtis McCully https://orcid.org/0000-0001-5807-7893
László Molnár https://orcid.org/0000-0002-8159-1599
Thomas Moore https://orcid.org/0000-0001-8385-3727
Pierre Mourier https://orcid.org/0000-0001-8078-6901
Anya E. Nugent https://orcid.org/0000-0002-2028-9329
David O'Neill https://orcid.org/0009-0001-1554-1868
Hugh Roxburgh https://orcid.org/0009-0001-6992-0898
Koji Shukawa https://orcid.org/0000-0002-2798-2943
Stephen J. Smartt https://orcid.org/0000-0002-8229-1731
Nathan Smith https://orcid.org/0000-0001-5510-2424
Ken W. Smith https://orcid.org/0000-0001-9535-3199
Bhagya M. Subrayan https://orcid.org/0000-0001-8073-8731
Sebastian Vergara Carrasco https://orcid.org/0009-0007-0282-7422
V. Ashley Villar https://orcid.org/0000-0002-5814-4061
József Vinkó https://orcid.org/0000-0001-8764-7832
Tal Wasserman https://orcid.org/0009-0005-7414-3965
Yossef Zenati https://orcid.org/0000-0002-0632-8897
Erez A. Zimmerman https://orcid.org/0000-0001-8985-2493

References

Aldering, G., Antilogus, P., Bailey, S., et al. 2006, ApJ, 650, 510
Amati, L. 2006, MNRAS, 372, 233
Arcavi, I. 2017, in Handbook of Supernovae, ed. A. W. Alsabti & P. Murdin (Springer), 239
Arnett, W. D. 1980, ApJ, 237, 541
Arnett, W. D. 1982, ApJ, 253, 785
Astropy Collaboration, Robitaille, T. P., Tollerud, E. J., et al. 2013, A&A, 558, A33
Astropy Collaboration, Price-Whelan, A. M., Sipőcz, B. M., et al. 2018, AJ, 156, 123
Astropy Collaboration, Price-Whelan, A. M., Lim, P. L., et al. 2022, ApJ, 935, 167
Atwood, W. B., Abdo, A. A., Ackermann, M., et al. 2009, ApJ, 697, 1071
Avakyan, A., Neumann, M., Zainab, A., et al. 2023, A&A, 675, A199
Balberg, S., & Loeb, A. 2011, MNRAS, 414, 1715
Barna, B., Nagy, A. P., Bora, Z., et al. 2023, A&A, 677, A183
Bell, K. J., & Higgins, M. E. 2022, TESS_PRF: Display the TESS pixel response function, Astrophysics Source Code Library, ascl:2207.008
Bellm, E. C., Kulkarni, S. R., Graham, M. J., et al. 2019, PASP, 131, 018002
Bersten, M. C., Folatelli, G., García, F., et al. 2018, Natur, 554, 497
Bilinski, C., Smith, N., Li, W., et al. 2015, MNRAS, 450, 246
Bilinski, C., Smith, N., Williams, G. G., et al. 2024, MNRAS, 529, 1104
Breeveld, A. A., Landsman, W., Holland, S. T., et al. 2011, AIPC, 1358, 373
Brown, P. J., Breeveld, A. A., Holland, S., Kuin, P., & Pritchard, T. 2014, A&SS, 354, 89
Brown, T. M., Baliber, N., Bianco, F. B., et al. 2013, PASP, 125, 1031
Calzavara, A. J., & Matzner, C. D. 2004, MNRAS, 351, 694
Chambers, K. C., Magnier, E. A., Metcalfe, N., et al. 2016, arXiv:1612.05560
Chandra, P., Chevalier, R. A., Chugai, N., Fransson, C., & Soderberg, A. M. 2015, ApJ, 810, 32
Chandra, P., Chevalier, R. A., James, N. J. H., & Fox, O. D. 2022, MNRAS, 517, 4151
Chatzopoulos, E., Wheeler, J. C., & Vinko, J. 2012, ApJ, 746, 121
Chatzopoulos, E., Wheeler, J. C., Vinko, J., Horvath, Z. L., & Nagy, A. 2013, ApJ, 773, 76
Chatzopoulos, E., Wheeler, J. C., Vinko, J., et al. 2011, ApJ, 729, 143
Chevalier, R. A., & Irwin, C. M. 2011, ApJL, 729, L6
Chevalier, R. A., & Irwin, C. M. 2012, ApJL, 747, L17
Christensen, E., Drake, A. J., Djorgovski, S. G., et al. 2009, CBET, 2106, 1
Chugai, N. N., Chevalier, R. A., & Lundqvist, P. 2004, MNRAS, 355, 627
Colgate, S. A., & McKee, C. 1969, ApJ, 157, 623
Couch, S. M., Pooley, D., Wheeler, J. C., & Milosavljević, M. 2011, ApJ, 727, 104
Dessart, L., Audit, E., & Hillier, D. J. 2015, MNRAS, 449, 4304
Drake, A. J., Djorgovski, S. G., Prieto, J. L., et al. 2010, ApJL, 718, L127
Drake, A. J., Mahabal, A. A., Djorgovski, S. G., et al. 2009, ATel, 2359, 1
Drout, M. R., Chornock, R., Soderberg, A. M., et al. 2014, ApJ, 794, 23
Duffell, P. C., & Ho, A. Y. Q. 2020, ApJ, 900, 193
Elias-Rosa, N., Van Dyk, S. D., Benetti, S., et al. 2018, ApJ, 860, 68
Ercolino, A., Jin, H., Langer, N., et al. 2026, A&A, 706, 169
Falk, S. W. 1978, ApJL, 225, L133
Fausnaugh, M. M., Jayaraman, R., Vanderspek, R., et al. 2023, RNAAS, 7, 56
Fausnaugh, M. M., Vallely, P. J., Tucker, M. A., et al. 2023, ApJ, 956, 108
Fox, O. D., Chevalier, R. A., Dwek, E., et al. 2010, ApJ, 725, 1768
Fox, O. D., Fransson, C., Smith, N., et al. 2020, MNRAS, 498, 517
Gaia Collaboration, Prusti, T., de Bruijne, J. H. J., et al. 2016, A&A, 595, A1
Gal-Yam, A. 2012, Sci, 337, 927
Gal-Yam, A. 2019, ARA&A, 57, 305
Gal-Yam, A., & Leonard, D. C. 2009, Natur, 458, 865
Gal-Yam, A., Leonard, D. C., Fox, D. B., et al. 2007, ApJ, 656, 372
Garnavich, P. M., Tucker, B. E., Rest, A., et al. 2016, ApJ, 820, 23
Gehrels, N., Chincarini, G., Giommi, P., et al. 2004, ApJ, 611, 1005
Gezari, S., Jones, D. O., Sanders, N. E., et al. 2015, ApJ, 804, 28
Ginsburg, A., Sipőcz, B. M., Brasseur, C. E., et al. 2019, AJ, 157, 98
Goldberg, J. A., Jiang, Y.-F., Bildsten, L., et al. 2022a, ApJ, 929, 156
Goldberg, J. A., Jiang, Y.-F., Bildsten, L., et al. 2022b, ApJ, 933, 164
Goldberg, J. A., Jiang, Y.-F., Bildsten, L., & Cantiello, M. 2026, ApJL, 998, L10
Goldstein, A., Cleveland, W. H., & Kocevski, D. 2023, Fermi Gamma-ray Data Tools: v2.0.0, GitHub, https://github.com/USRA-STI/gdt-fermi
Goldstein, A., Cleveland, W. H., & Kocevski, D. 2024, Gamma-ray Data Tools Core Package: v2.0.4, GitHub, https://github.com/USRA-STI/gdt-core
Górski, K. M., Hivon, E., Banday, A. J., et al. 2005, ApJ, 622, 759
Gruber, D., Goldstein, A., Weller von Ahlefeld, V., et al. 2014, ApJS, 211, 12
Guillochon, J., Nicholl, M., Villar, V. A., et al. 2018, ApJS, 236, 6
Güver, T., & Özel, F. 2009, MNRAS, 400, 2050
Hamuy, M. 2003, ApJ, 582, 905
Hamuy, M., Phillips, M. M., Suntzeff, N. B., et al. 2003, Natur, 424, 651
Harris, C. R., Millman, K. J., van der Walt, S. J., et al. 2020, Natur, 585, 357
Heussaff, V., Atteia, J.-L., & Zolnierowski, Y. 2013, A&A, 557, A100
Higson, E., Handley, W., Hobson, M., & Lasenby, A. 2019, S&C, 29, 891
Hiramatsu, D., Berger, E., Gomez, S., et al. 2024, arXiv:2411.07287
Hocdé, V., Smolec, R., Moskalik, P., Ziółkowska, O., & Singh Rathour, R. 2023, A&A, 671, A157
Howell, D. A. 2017, in Handbook of Supernovae, ed. A. W. Alsabti & P. Murdin (Springer), 431
Hunter, J. D. 2007, CSE, 9, 90
Irani, I., Morag, J., Gal-Yam, A., et al. 2024, ApJ, 970, 96
Irwin, C. M., & Hotokezaka, K. 2025, MNRAS, 543, 2917
Irwin, C. M., Linial, I., Nakar, E., Piran, T., & Sari, R. 2021, MNRAS, 508, 5766
Jayaraman, R., Fausnaugh, M., Ricker, G. R., Vanderspek, R., & Mo, G. 2024, ApJ, 972, 162
Jiang, B., Jiang, S., & Ashley Villar, V. 2020, RNAAS, 4, 16
Kasen, D. 2010, ApJ, 708, 1025
Katsuda, S., Maeda, K., Nozawa, T., Pooley, D., & Immler, S. 2014, ApJ, 780, 184
Katz, B., Budnik, R., & Waxman, E. 2010, ApJ, 716, 781
Khatami, D. K., & Kasen, D. N. 2024, ApJ, 972, 140
Kochanek, C. S., Shappee, B. J., Stanek, K. Z., et al. 2017, PASP, 129, 104502
Lane, Z. G. 2025, AstroColour v1.3.0, GitHub, https://github.com/ZacharyLane1204/AstroColour.git
Li, W., Leaman, J., Chornock, R., et al. 2011, MNRAS, 412, 1441
Magnier, E. A., Schlafly, E. F., Finkbeiner, D. P., et al. 2020, ApJS, 251, 6
Masci, F. J., Laher, R. R., Rusholme, B., et al. 2019, PASP, 131, 018003
Masci, F. J., Laher, R. R., Rusholme, B., et al. 2023, arXiv:2305.16279
Matzner, C. D., Levin, Y., & Ro, S. 2013, ApJ, 779, 60
Matzner, C. D., & McKee, C. F. 1999, ApJ, 510, 379
Mauerhan, J. C., Smith, N., Filippenko, A. V., et al. 2013, MNRAS, 430, 1801
McCully, C., Volgenau, N. H., Harbeck, D.-R., et al. 2018, SPIE, 10707, 107070K
McKinney, W. 2010, in Proc. of the 9th Python in Science Conf., ed. S. van der Walt & J. Millman, 56
Meegan, C., Lichti, G., Bhat, P. N., et al. 2009, ApJ, 702, 791
Moran, S., Fraser, M., Kotak, R., et al. 2023, A&A, 669, A51
Moriya, T. J., Galbany, L., Jiménez-Palau, C., et al. 2023, A&A, 677, A20
Moriya, T. J., Maeda, K., Taddia, F., et al. 2013, MNRAS, 435, 1520
Moroianu, A., Wen, L., James, C. W., et al. 2023, NatAs, 7, 579
Nagao, T., Maeda, K., & Ouchi, R. 2020, MNRAS, 497, 5395
Narayana Bhat, P., Meegan, C. A., von Kienlin, A., et al. 2016, ApJS, 223, 28

Neumann, M., Avakyan, A., Doroshenko, V., & Santangelo, A. 2023, A&A, 677, A134
Nugent, A. E., Villar, V. A., Gagliano, A., et al. 2026, ApJ, 997, 38
Nyholm, A., Sollerman, J., Tartaglia, L., et al. 2020, A&A, 637, A73
Ofek, E. O., Arcavi, I., Tal, D., et al. 2014a, ApJ, 788, 154
Ofek, E. O., Cameron, P. B., Kasliwal, M. M., et al. 2007, ApJL, 659, L13
Ofek, E. O., Sullivan, M., Cenko, S. B., et al. 2013, Natur, 494, 65
Ofek, E. O., Sullivan, M., Shaviv, N. J., et al. 2014b, ApJ, 789, 104
Ofek, E. O., Zackay, B., Gal-Yam, A., et al. 2019, PASP, 131, 054204
Ofek, E. O., Zoglauer, A., Boggs, S. E., et al. 2014c, ApJ, 781, 42
Perley, D. A., Ho, A. Y. Q., Fausnaugh, M., et al. 2025, MNRAS, 537, 2362
Piran, T., Nakar, E., Mazzali, P., & Pian, E. 2019, ApJL, 871, L25
Poolakkil, S., Preece, R., Fletcher, C., et al. 2021, ApJ, 913, 60
Quimby, R. M., De Cia, A., Gal-Yam, A., et al. 2018, ApJ, 855, 2
Ransome, C. L., & Villar, V. A. 2025, ApJ, 987, 13
Rest, A., Foley, R. J., Gezari, S., et al. 2011, ApJ, 729, 88
Rest, S., Rest, A., Kilpatrick, C. D., et al. 2025, ApJ, 979, 114
Ricker, G. R., Winn, J. N., Vanderspek, R., et al. 2014, JATIS, 1, 014003
Ridden-Harper, R., Rest, A., Hounsell, R., et al. 2021, arXiv:2111.15006
Roxburgh, H., Ridden-Harper, R., Lane, Z. G., et al. 2024, ApJ, 963, 89
Roxburgh, H., Ridden-Harper, R., Moore, A., et al. 2025, AJ, 170, 186
Schlafly, E. F., & Finkbeiner, D. P. 2011, ApJ, 737, 103
Schlegel, E. M. 1990, MNRAS, 244, 269
Schulze, S., Krühler, T., Leloudas, G., et al. 2018, MNRAS, 473, 1258
Schulze, S., Yaron, O., Sollerman, J., et al. 2021, ApJS, 255, 29
Shahbandeh, M., Fox, O. D., Temim, T., et al. 2025, ApJ, 985, 262
Sharma, Y., Sollerman, J., Fremling, C., et al. 2023, ApJ, 948, 52
Smith, K. W., Smartt, S. J., Young, D. R., et al. 2020, PASP, 132, 085002
Smith, N. 2014, ARA&A, 52, 487
Smith, N. 2017, in Handbook of Supernovae, ed. A. W. Alsabti & P. Murdin (Springer), 403
Smith, N. 2026, Encyclopedia of Astrophysics, Vol. 2 (Elsevier), 508
Smith, N., & Andrews, J. E. 2020, MNRAS, 499, 3544
Smith, N., Andrews, J. E., Milne, P., et al. 2024, MNRAS, 530, 405
Smith, N., & Arnett, W. D. 2014, ApJ, 785, 82
Smith, N., Chornock, R., Li, W., et al. 2008, ApJ, 686, 467
Smith, N., Chornock, R., Silverman, J. M., Filippenko, A. V., & Foley, R. J. 2010a, ApJ, 709, 856
Smith, N., & McCray, R. 2007, ApJL, 671, L17
Smith, N., Li, W., Foley, R. J., et al. 2007, ApJ, 666, 1116
Smith, N., Silverman, J. M., Chornock, R., et al. 2009, ApJ, 695, 1334
Smith, N., Miller, A., Li, W., et al. 2010b, AJ, 139, 1451
Smith, N., Li, W., Miller, A. A., et al. 2011, ApJ, 732, 63
Smith, N., Kilpatrick, C. D., Mauerhan, J. C., et al. 2017, MNRAS, 466, 3021
Soderberg, A. M., Berger, E., Page, K. L., et al. 2008, Natur, 453, 469
Speagle, J. S. 2020, MNRAS, 493, 3132
Srinivasaragavan, G. P., Hamidani, H., Schroeder, G., et al. 2025, ApJL, 988, L60
Stanek, K. Z. 2019, TNSTR, 2019-2492, 1
Strotjohann, N. L., Ofek, E. O., Gal-Yam, A., et al. 2021, ApJ, 907, 99
STScI Development Team 2013, pysynphot: Synthetic photometry software package, Astrophysics Source Code Library, ascl:1303.023
Suzuki, A., Moriya, T. J., & Takiwaki, T. 2019, ApJ, 887, 249
Suzuki, A., Nicholl, M., Moriya, T. J., & Takiwaki, T. 2021, ApJ, 908, 99
TESS Team 2022, TESS Calibrated Full Frame Images: All Sectors, STScI/MAST, doi:10.17909/0CP4-2J79
Tinyanont, S., Ridden-Harper, R., Foley, R. J., et al. 2022, MNRAS, 512, 2777
Tonry, J. L., Denneau, L., Heinze, A. N., et al. 2018a, PASP, 130, 064505
Tonry, J. L., Denneau, L., Flewelling, H., et al. 2018b, ApJ, 867, 105
Tsuna, D., Takei, Y., Kuriyama, N., & Shigeyama, T. 2021, PASJ, 73, 1128
Tsvetkov, D., Pavlyuk, N., Dodin, A., et al. 2024, AN, 345, e20230166
Vanderspek, R., Doty, J., Fausnaugh, M., et al. 2018, TESS Instrument Handbook, Tech. rep., Kavli Institute for Astrophysics and Space Science, Massachusetts Institute of Technology
Villar, V. A., Berger, E., Metzger, B. D., & Guillochon, J. 2017, ApJ, 849, 70
Virtanen, P., Gommers, R., Oliphant, T. E., et al. 2020, NatMe, 17, 261
Vishniac, E. T. 1983, ApJ, 274, 152
von Kienlin, A., Meegan, C. A., Paciesas, W. S., et al. 2014, ApJS, 211, 13
von Kienlin, A., Meegan, C. A., Paciesas, W. S., et al. 2020, ApJ, 893, 46
Wang, Q., Armstrong, P., Zenati, Y., et al. 2023, ApJL, 943, L15
Wang, Q., Rest, A., Dimitriadis, G., et al. 2024, ApJ, 962, 17
Wasserman, T., Sapir, N., Szabo, P., & Waxman, E. 2025, ApJ, 993, 46
Wasserman, T., & Waxman, E. 2026, ApJ, 998, 247
Waters, C. Z., Magnier, E. A., Price, P. A., et al. 2020, ApJS, 251, 4
Waxman, E., & Katz, B. 2017, in Handbook of Supernovae, ed. A. W. Alsabti & P. Murdin (Springer), 967
Zegarelli, A., Guetta, D., Celli, S., et al. 2024, A&A, 690, A187
Zonca, A., Singer, L., Lenz, D., et al. 2019, JOSS, 4, 1298